PLOS ONE

RESEARCH ARTICLE

Numerical modelling of blood rheology and platelet activation through a stenosed left coronary artery bifurcation

David G. Owen*, Diana C. de Oliveira☯, Emma K. Neale☯, Duncan E. T. Shepherd☯, Daniel M. Espino☯

Department of Mechanical Engineering, University of Birmingham, Birmingham, United Kingdom

☯ These authors contributed equally to this work.
* dgo452@bham.ac.uk

Citation: Owen DG, de Oliveira DC, Neale EK, Shepherd DET, Espino DM (2021) Numerical modelling of blood rheology and platelet activation through a stenosed left coronary artery bifurcation. PLoS ONE 16(11): e0259196. https://doi.org/10.1371/journal.pone.0259196

Editor: Fang-Bao Tian, University of New South Wales, AUSTRALIA

Received: July 28, 2021

Accepted: October 14, 2021

Published: November 3, 2021

Data Availability Statement: All relevant data are within the manuscript and its Supporting information files.

Funding: D.G.O. was funded by the Engineering and Physical Sciences Research Council (EPSRC; grant no. EP/N509590/1). The funders had no role in study design, data collection and analysis, decision to publish, or preparation of the manuscript.

Competing interests: The authors have declared that no competing interests exist.

Abstract

Coronary bifurcations are prone to atherosclerotic plaque growth, experiencing regions of reduced wall shear stress (WSS) and increased platelet adhesion. This study compares effects across different rheological approaches on hemodynamics, combined with a shear stress exposure history model of platelets within a stenosed porcine bifurcation. Simulations used both single/multiphase blood models to determine which approach best predicts phenomena associated with atherosclerosis and atherothrombosis. A novel Lagrangian platelet tracking model was used to evaluate residence time and shear history of platelets indicating likely regions of thrombus formation. Results show a decrease in area of regions with pathologically low time-averaged WSS with the use of multiphase models, particularly in a stenotic bifurcation. Significant non-Newtonian effects were observed due to low-shear and varying hematocrit levels found on the outer walls of the bifurcation and distal to the stenosis. Platelet residence time increased 11% in the stenosed artery, with exposure times to low-shear sufficient for red blood cell aggregation (>1.5 s). increasing the risk of thrombosis. This shows stenotic artery hemodynamics are inherently non-Newtonian and multiphase, with variations in hematocrit (0.163–0.617) and elevated vorticity distal to stenosis (+15%) impairing the function of the endothelium via reduced time-averaged WSS regions, rheological properties and platelet activation/adhesion.

Introduction

Cardiovascular diseases were responsible for an estimated 18.8 million deaths in 2017 [1], with heart disease being the leading cause of death in the USA in the same year [2]. Of particular relevance to cardiovascular health are the coronary arteries, two major blood vessels which bifurcate into multiple smaller branches. The coronary arteries have been associated with several clinical pathologies, including atherosclerotic plaques/lesions [3, 4], arterial stiffening [5] and increased thrombosis [6] (clot formation). Atherosclerosis is the development of fatty plaques within the artery wall, with their onset and progression associated with regions of low

time-averaged wall shear stress [7] (TAWSS) occurring around the branching of the artery [8] or distal to regions of stenosis [9]. In addition to plaque rupture causing myocardial infarction or sudden death [2], the altered hemodynamics arising from inflammatory plaque growth also impacts the behaviour and activation of platelets; catalysing plaque/fibrin growth through increased platelet adhesion and increased risk of thrombus formation [10] (atherothrombosis), with a detailed review of these phenomena provided by Davi and Patrono [11].

Computational fluid dynamics (CFD) is a useful tool to study vascular pathologies and is capable of predicting the location and progression of coronary atherosclerotic plaques [12], growth/rupture of aneurysms [13] and microscopic thrombus growth [14]. The branching of the coronary arteries results in low-shear and stagnant/recirculation environments occurring on the outer walls [15], being common sites for plaque growth and hence stenosis to occur. The realistic simulation of blood flow in these regions is crucial for accurate hemodynamic predictions and hence the understanding of disease mechanisms. There are multiple fundamentally different approaches to blood rheology [16], all based on fitting constituent equations to differing sets of experimental viscometer data [17]. Blood is a multiphase fluid, comprised predominantly of a dilute suspension of red blood cells (RBC) within a plasma continuum [18]. Rheological properties depend on fluid shear rates, the concentration of RBC [19] (hematocrit) and crucially the aggregation of individual RBC into a rouleaux, which is a key factor in non-Newtonian behaviour. Rouleaux formation requires prolonged exposure to low-shear rates [20] ($<50\ s^{-1}$), and as is inherently a microscopic phenomenon [21]. As there are approximately 5×10^6 RBC per mm^3 of blood [22], it is impossible to simulate this phenomenon for large arteries with current computational power. Shear-rates in larger arteries are conventionally considered to be sufficiently high for rouleaux formation to be negligible, in which case a more simplistic approach is to assume blood to be a homogeneous single-phase fluid, with constant density and either a constant [23] (Newtonian) or a shear-thinning (non-Newtonian) viscosity [24]. However, as a low-shear environment is commonly associated with disease, the extent to which this assumption oversimplifies crucial behaviour is contended [25]. As macroscale multiphase models do not simulate individual RBC, representing the rheological effects of aggregation and rouleaux formation is an ongoing challenge. However, the recent 5-parameter Modified Krieger Model (MKM5), is based upon the Krieger model for suspensions and attempts to incorporate the effect of aggregation on the viscosity of blood [26].

Many of the studies that focus on the impact of different types of rheology in coronary artery hemodynamics employ healthy geometries, and assume blood as a single-phase fluid [27–29], with fewer studies assessing the effects of multiphase models in coronary hemodynamics [30, 31]. Despite significant evidence on the non-Newtonian effects occurring around the coronary bifurcation, and the importance of hematocrit on the properties of blood, to date there is no conclusive study comparing these effects on parameters associated with the progression of atherosclerosis, and the subsequent impact on atherothrombosis/platelet activation.

The present study aims to compare the impact of different rheological assumptions on a diseased left coronary bifurcation (at the level of the left anterior descending artery, LAD, and the left circumflex artery, LCx). In particular, the prediction of blood flow in the low-shear environment distal to the bifurcation/stenotic regions, including the aggregatory potential of RBC via low-shear residence time and variations in hematocrit. Furthermore, the effect of stenosis on the transport/activation of platelets will be considered for a multiphase model, using a novel Lagrangian platelet simulation to evaluate trajectories, residence times and level of activation. A total of four rheological models were considered: single-phase Newtonian (SN); single-phase Carreau (SC) multiphase Newtonian (MN); and multiphase MKM5.

Methods

Geometry

Coronary bifurcation. The vessel geometry was constructed using a centreline profile from an *ex vivo* sample of healthy porcine left main coronary artery bifurcation (LAD-LCx) from Fresh Tissue Supplies, Horsham, UK. This was scaled to match human physiological dimensions [32] using SolidWorks (SolidWorks, Dassault Systèmes, Vèlizy-Villacublay, France), and is shown in Fig 1. The total length of the artery is 70 mm, with a branch angle of approximately 72˚, an inlet diameter of 4.5 mm, and outlet diameters of the LAD and LCx branch being 3 mm and 2 mm, respectively. The reduction in circular lumen diameter was achieved via linear-interpolation between the inlet-outlet resulting in a gradual tapering. To avoid any unwanted entrance/exit effects on the hemodynamics of the bifurcation, the inlets and outlets have been extended 15 mm using a constant diameter.

Diseased coronary bifurcation. A common coronary artery disease is the growth of atherosclerotic plaques within the lumen surface resulting in stenosis and a reduction in lumen diameter. Based upon an *in vivo* study of 140 patients, the most common occurring stenosis in coronary artery bifurcations is a continuous and diffuse plaque in both the LAD and LCx branches [33]. Stenosis can be defined as the reduction in lumen diameter due to plaque

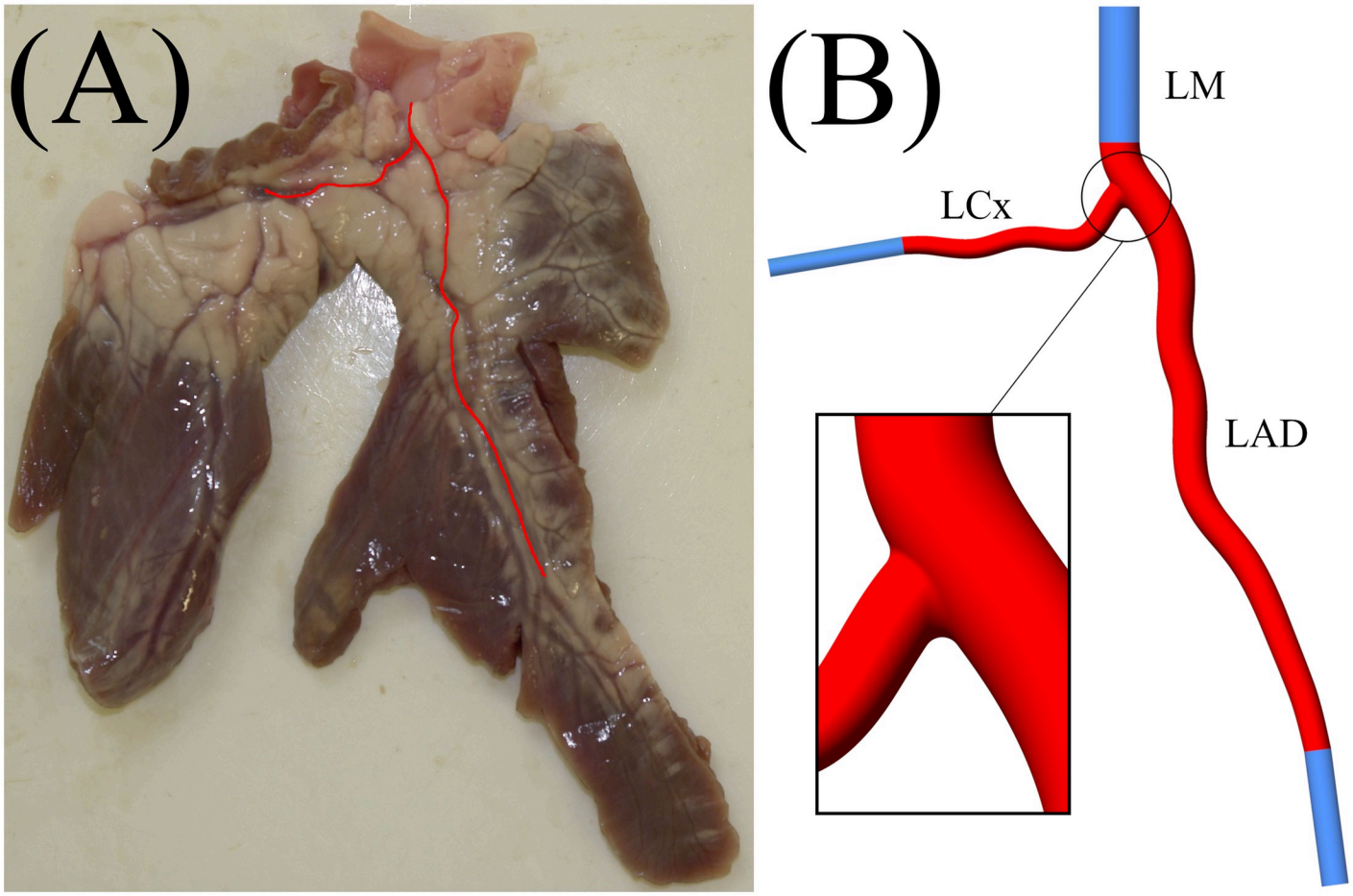

Fig 1. (A)—Porcine *ex vivo* heart segment, with coronary geometry marked in red. (B) Coronary artery bifurcation geometry including domain extensions shown in blue (LAD, left anterior descending artery; LCx, left circumflex artery; LM, left main coronary artery).

https://doi.org/10.1371/journal.pone.0259196.g001

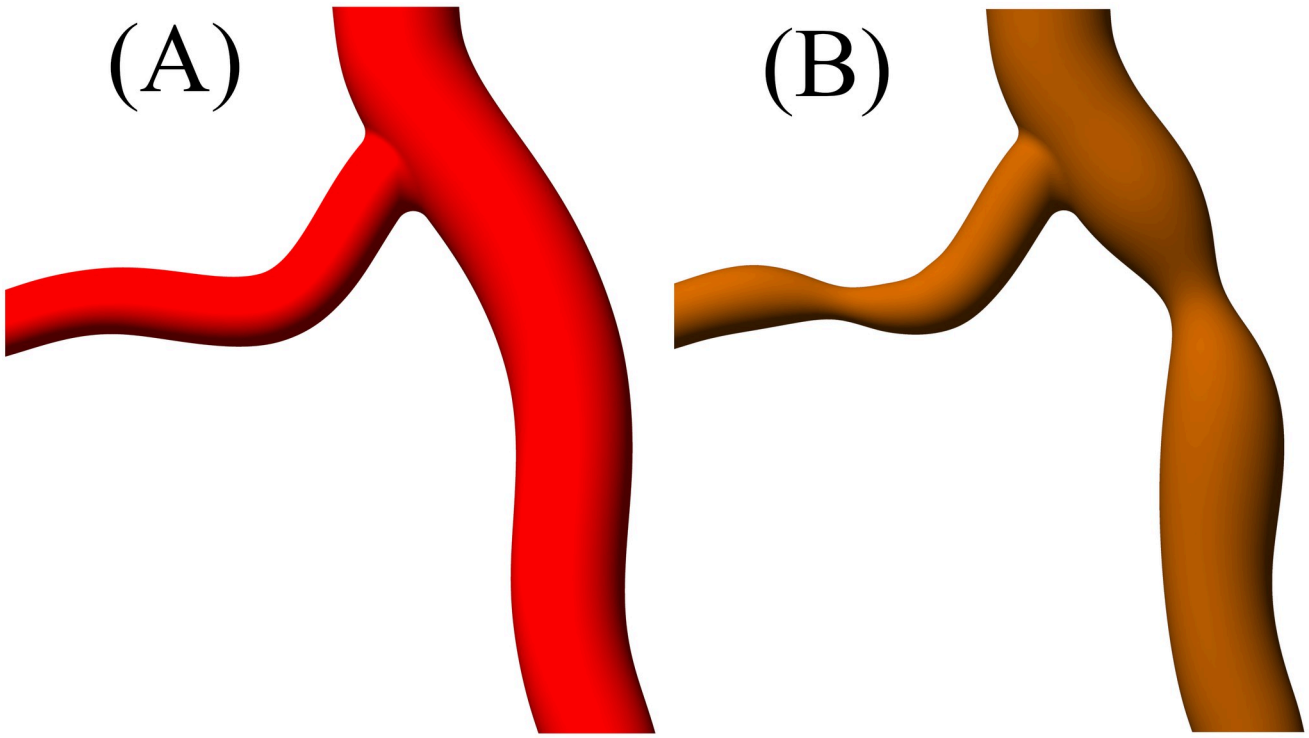

Fig 2. Comparison between (A) healthy and (B) diseased arterial bifurcation with stenosis.

https://doi.org/10.1371/journal.pone.0259196.g002

formation (Eq 1), with this study using a 50% stenosis.

$$S_p = \frac{D_{healthy} - D_{min}}{D_{healthy}} \tag{1}$$

where S_p is the percentage stenosis, $D_{healthy}$ is the diameter before the plaque and D_{min} is the minimum arterial dimeter at the point of maximum stenosis. A comparison between the healthy/diseased arterial geometry is shown in Fig 2.

Rheological models

Whole blood exhibits significant non-Newtonian properties [34], with a viscosity that depends on shear rate (Eq 2) and hematocrit (red blood cell concentration) as well as a variety of other mechanical/biological factors [16].

$$\dot{\gamma} = \sqrt{2D_{ij} \cdot D_{ij}} \tag{2}$$

where $\dot{\gamma}$ is the shear rate of the fluid, D is the strain rate tensor with i,j = 1,2,3 as the inner products. This study examines four different rheological models, consisting of two single-phase models (which consider blood a single homogenous fluid), and two multiphase models (which consider blood as a dilute suspension of RBC within a plasma continuum). Of the two single-phase models, one assumes blood to be Newtonian [35] with constant viscosity (Single Newtonian, SN), and the other uses a shear dependant Carreau [36] viscosity definition (Single Carreau, SC). Similarly for the two multiphase models, one uses a Newtonian approach, where the viscosity of each phase is constant (Multi Newtonian, MN) and the other uses a modified

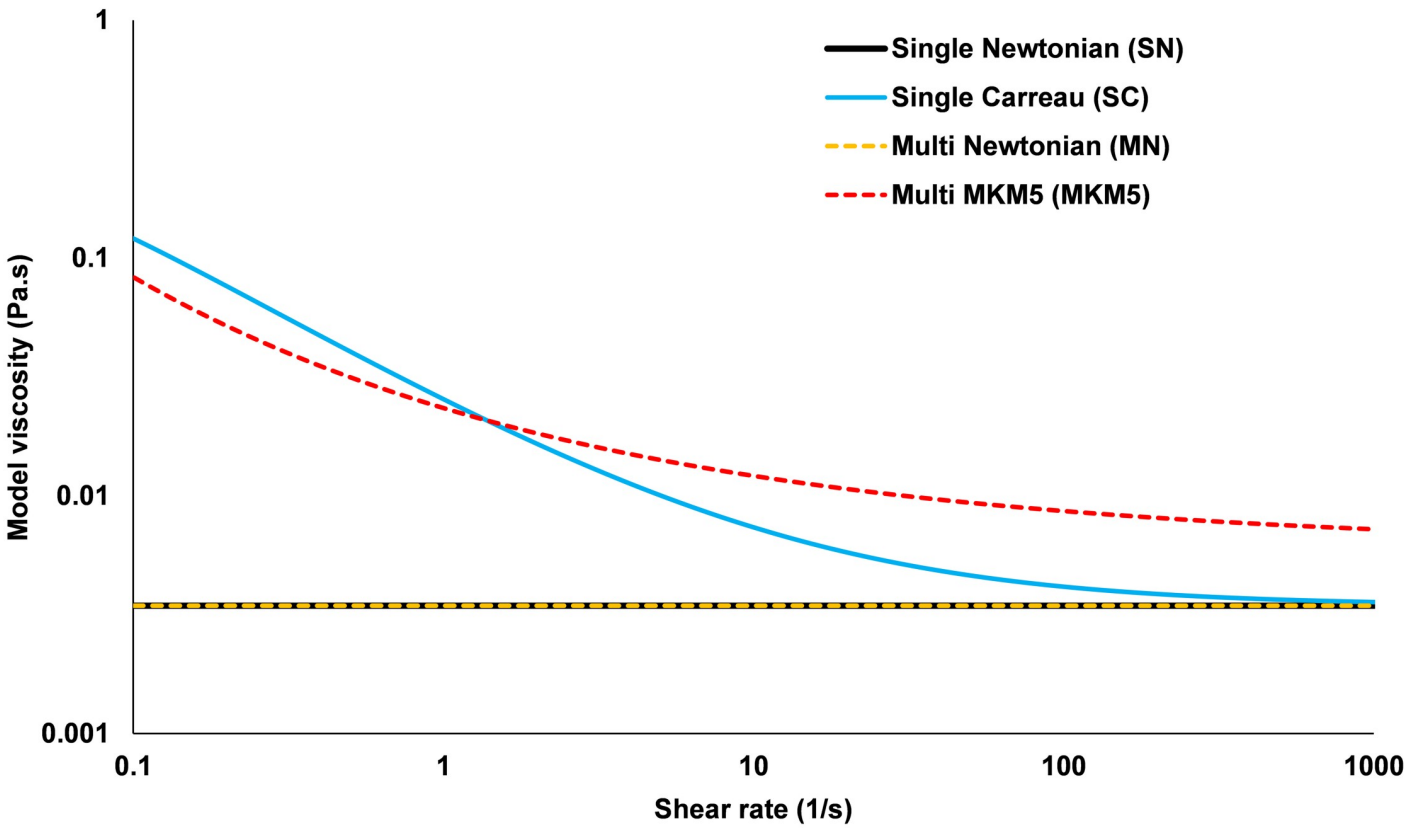

Fig 3. Apparent blood viscosity versus shear rate for the four rheological models (Multiphase models use a Hematocrit of 0.45).

https://doi.org/10.1371/journal.pone.0259196.g003

Krieger model with 5 parameters [26] (MKM5) which allows RBC viscosity to vary with both shear forces and hematocrit. The viscosity of whole blood at varying physiological shear rates for each of the four models is given in Fig 3. The accompanying mathematical definitions and coefficients for each model are provided in Table 1.

In Table 1, μ_{rbc} is the viscosity of the RBC, μ_p is the viscosity of plasma, $\emptyset_{rbc}$ is the hematocrit and $\emptyset_{rbc,crit}$ is the critical hematocrit where the RBC no longer behave as a fluid. As the definitions in Table 1 are for the viscosities of whole blood, the viscous definitions required for the RBC in the MKM5 model can be inferred from a weighted average shown in Eq 3.

$$\mu_{rbc} = \frac{\mu_{blood} - (1 - \emptyset_{rbc})\mu_p}{\emptyset_{rbc}} \tag{3}$$

where μ_{blood} is the definition of MKM5 viscosity provided in Table 1. This equation was also used to calculate the Newtonian viscosity of the RBC based upon a hematocrit of 0.45 and a whole blood mixture viscosity of 3.45 mPa.s.

Numerical methods

Governing equations

The governing equations for the continuity of mass and momentum for the single and multiphase models are given in Table 2, including additional multiphase relationships. These equations were solved numerically using the commercial finite-volume solver Fluent (Ansys v20.1,

Table 1. Definitions for the rheological models.

Model	Viscosity definition (Pa.s)	Parameters
Single-phase Newtonian [35] (SN)	$\mu = 0.00345$	-
Single-phase Carreau [36] (SC)	$\mu = \mu_\infty + (\mu_0 - \mu_\infty)[1 + (\lambda\dot{\gamma})^2]^{\frac{n-1}{2}}$	$\mu_\infty = 0.00345$, $n = 0.25$
		$\mu_0 = 0.25$, $\lambda = 25$
Multiphase Newtonian (MN)	$\mu = \mu_{rbc}\emptyset_{rbc} + \mu_p(1 - \emptyset_{rbc})$	$\mu_{rbc} = 0.006163$
		$\mu_p = 0.00123$
Multiphase Modified Krieger Model 5 Parameters [30] (MKM5)	$\mu = \mu_p\left[1 - \frac{\emptyset_{rbc}}{\emptyset_{rbc,crit}}\right]^{-n}$	$\mu_p = 0.00123$
		$\emptyset_{rbc,crit} = 0.95$
	$n = \begin{cases} n_\infty \text{ if } \emptyset_{rbc} < 0.2 \\ n_\infty + n_{st} \text{ if } \emptyset_{rbc} > 0.2 \end{cases}$	$b = 8.78084$
		$c = 2.82354$
	$n_\infty = be^{-c\emptyset_{rbc}}, \quad n_{st} = \beta\gamma'^{-v}$	$\beta = 16.27775$
	$\gamma' = 1 + (\lambda\dot{\gamma})^{v_g}$	$v = 0.14275$
		$\lambda = 1252.64407$
		$v_g = 2$

https://doi.org/10.1371/journal.pone.0259196.t001

Ansys Inc., Canonsburg, PA, USA). The single-phase models assumed blood to be incompressible with a density [37] of $\rho = 1060$ kg/m^3. The transport and phase interactions of the multiphase models were implemented using an Eulerian-Eulerian mixture model similar to other cardiovascular models [38], which considers RBC as a dilute suspension within a Newtonian plasma continuum, with a comprehensive overview of this technique available elsewhere [30].

The momentum exchange coefficient between phases is derived from the RBC interfacial-area [39], and the viscous drag they experience, which is given by the Shiller-Naumann [40] model for spheres. The only external force considered was the virtual mass force, arising from the changing inertia of the plasma phase due to relative RBC acceleration. The lift due to shear is also not included due to limitations of numerical models at wide ranging Reynolds numbers/shear rates near the boundary [41] as well as only being recommended for sub-micron particles [42]. In both multiphase models, the density of plasma [17] and RBC [43] were set as $\rho_a = 1003$ kg/m^3 and $\rho_b = 1096$ kg/m^3, respectively. The hematocrit distribution of the domain and inlet was set at a uniform 45% based upon physiological ranges [44], however, the exact *in vivo* distribution is unknown.

Platelet modelling

To further evaluate the hemodynamics of the coronary bifurcation, platelets were released into the domain and tracked over multiple cardiac cycles to evaluate their path lines and physical properties. The platelets were considered as 2 μm diameter rigid spheres [45] with density $\rho_p = 1040$ kg/m^3, and were assumed not to impact the blood transport (one way interaction with fluid phases). The platelets path line is calculated by equating particle inertia to the sum of forces upon the particle from Eq 4.

$$\frac{d\vec{u_p}}{dt} = F_D\left(\vec{u} - \vec{u_p}\right) + \vec{F} \tag{4}$$

where $\vec{u}$ and $\vec{u_p}$ are the fluid and platelet velocity, respectively, F_D is the drag force (Eq 5) and $\vec{F}$ is the contribution of external forces.

$$F_D = \frac{18\mu}{\rho_p d_p^2}\frac{C_D Re}{24} \tag{5}$$

Table 2. Conservation of mass and momentum for the single and multiphase models, with the volume fraction and external force (virtual mass) definitions for the multiphase models.

Single-phase equations	
$\frac{\partial u_i}{\partial x_i} = 0$	where u is the velocity, x is the spatial coordinate, t is time, μ is fluid viscosity, ρ is fluid density and p is pressure.
$\frac{\partial u_i}{\partial t} + u_j \frac{\partial u_i}{\partial x_j} = \frac{\partial}{\partial x_j}\left(\mu \frac{\partial u_i}{\partial x_j}\right) - \frac{1}{\rho}\frac{\partial p}{\partial x_i}$	
Multiphase equations	
$\sum_{n=1}^{2} \emptyset_n = 1$	where $\emptyset$ is the volume fraction of each phase, a, b are the primary/secondary phases (plasma/RBC) respectively, ρ_b is the density of phase b, $\vec{v}_b$ is the velocity of phase b, p is pressure (shared by all phases), $\bar{\bar{\tau}}_b$ is the stress-strain tensor of phase b, K_{ab} is the interphase momentum exchange coefficient and $\vec{F}_{ext}$ are the external forces.
$\frac{\partial}{\partial t}(\emptyset_b \rho_b) + \nabla \cdot (\emptyset_b \rho_b \vec{v}_b) = 0$	
$\frac{\partial}{\partial t}(\emptyset_b \rho_b \vec{v}_b) + \nabla \cdot (\emptyset_b \rho_b \vec{v}_b \vec{v}_b) = -\emptyset_b \nabla \mathrm{p} + \nabla \cdot \bar{\bar{\tau}}_b + \sum_{a,b=1}^{2} K_{ab}(\vec{v}_a - \vec{v}_b) + \vec{F}_{ext}$	
$\vec{F}_{vm} = 0.5 \emptyset_b \rho_a \left(\frac{d_a \vec{v}_a}{dt} - \frac{d_b \vec{v}_b}{dt}\right)$	

https://doi.org/10.1371/journal.pone.0259196.t002

where d_p is platelet diameter, Re is the relative Reynolds number and C_D is the drag coefficient of the platelet defined in Eq 6, using coefficients over a range of Reynolds numbers determined by Morsi and Alexander [46].

$$C_D = \alpha_1 + \frac{\alpha_2}{Re} + \frac{\alpha_3}{Re^2} \tag{6}$$

Whilst the most significant force upon the platelets is viscous drag, other important forces when particle/fluid densities are similar are the pressure gradient and virtual mass forces (Eqs 7 and 8) acting upon the platelet and are given, respectively, by:

$$\overrightarrow{F_p} = \frac{\rho}{\rho_p} \overrightarrow{u_p} \nabla \vec{u} \tag{7}$$

$$\overrightarrow{F_{vmp}} = \frac{\rho}{2\rho_p}\left(\overrightarrow{u_p} \nabla \vec{u} - \frac{d\,\overrightarrow{u_p}}{dt}\right) \tag{8}$$

Additional forces such as those due to buoyancy, Magnus force, and Brownian motion are not included as they were assumed negligible [47]. The time dependant shear history of the platelets was evaluated using the approach first presented by Bluestein *et al.* [48], which determines the 'level of activation' (LOA) via the cumulative sum of a platelets exposure time (Δt) to shear stresses within the blood (Eq 9).

$$L.O.A = \sum [(\mu \cdot \dot{\gamma}) \cdot \Delta t] \tag{9}$$

This relativistic measure can identify potential regions for the activation/aggregation of platelets, with an elevated LOA being defined as values >66th percentile from the total range. Platelets were released in 8 separate groups from the physiological inlet at 0.1 s intervals (Fig 4), with each mesh element seeding one platelet, for a total of 13439 per release which approximates the normal human concentration [49]. The platelets were realised after 3 cardiac cycles (2.4 s) had been completed and were tracked through the flow field for a total period of 4 s (up to 6.4 s).

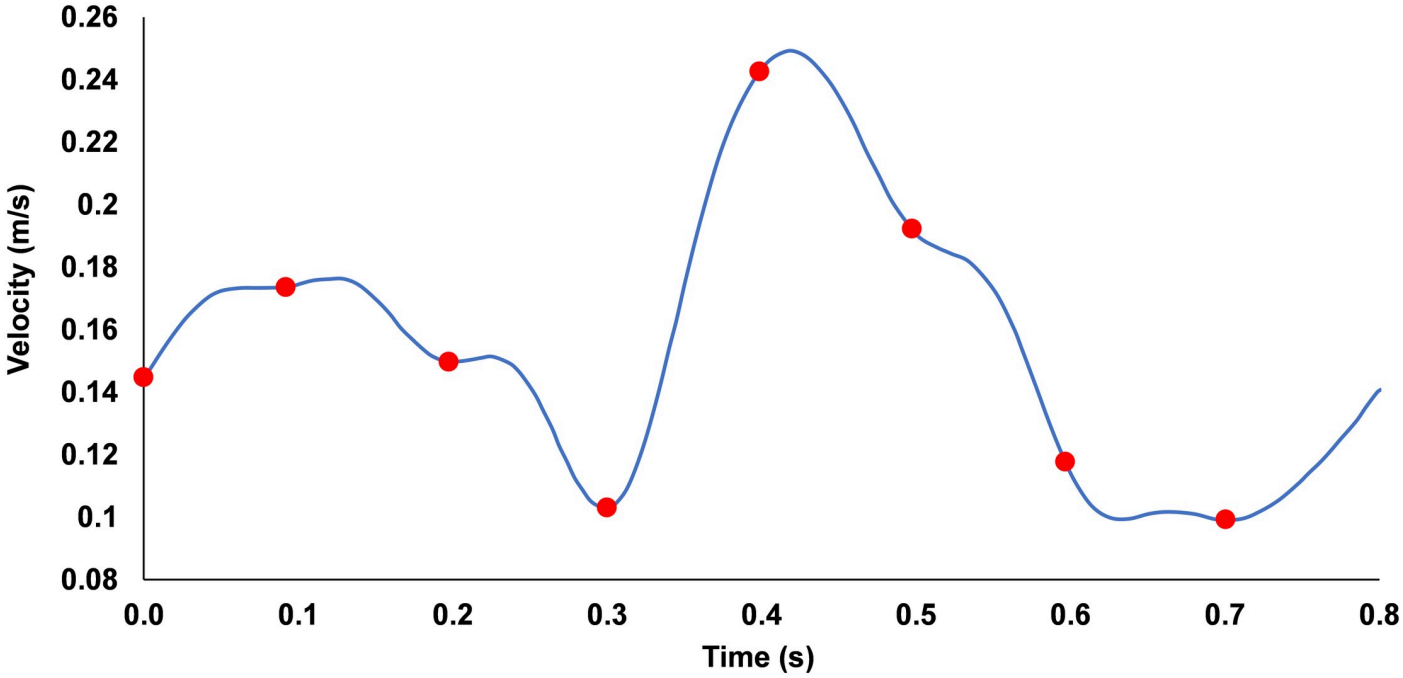

Fig 4. Variation of inlet velocity against time applied to the coronary artery, red dots indicate the 0.1 s intervals during which platelets were released into flow.

https://doi.org/10.1371/journal.pone.0259196.g004

Boundary conditions

Inlet and outlet. A typical physiological left main coronary velocity waveform [50] (Fig 4) was fitted to a Fourier series and scaled to match the model size, with a Reynolds number range from 277–691.

A parabolic velocity profile describing developed laminar flow [51] was implemented to the waveform in Fig 4 using Eq 10.

$$u(r,t) = 2V(t)\left[1 - \left(\frac{r^2}{R^2}\right)\right] \tag{10}$$

where $V(t)$ is the inlet velocity waveform, r is the radial position at the inlet and R is the maximum radius of the inlet (4.5 mm). A constant pressure of 120 mmHg (16 kPa) which approximates with mean systolic blood pressure [52] was applied at the outlets.

Hemodynamic parameters

To compare the differences in the hemodynamics arising from the different geometries and rheology models, parameters commonly associated with the assessment of atherosclerosis are defined in Eqs 11–17.

Wall shear stress (WSS) is the force exerted by the flow of blood over the artery surface, and is a function of the viscosity and velocity gradient of the fluid, defined in Eq 11.

$$\tau_w = \mu \frac{\partial u_t}{\partial n}\Big|_{wall} \tag{11}$$

where τ_w is wall shear stress, u_t is tangential wall velocity and n is unit vector perpendicular to the wall. The WSS fluctuates throughout the cardiac cycle, and so averaging WSS over the

cycle can better represent the flow conditions. Time-averaged wall shear stress (TAWSS) (Eq 12) has been extensively correlated to the onset and progression of CVD such as atherosclerosis, with a magnitude <1 Pa considered atherodegenerative based upon multiple *in vivo* and *in vitro* studies [7, 53, 54].

$$\bar{\tau}_w = \frac{1}{T}\int_0^T |\tau_w|\, dt \tag{12}$$

where $\bar{\tau}_w$ is the TAWSS and T is the length of one cardiac cycle. The oscillatory shear index (OSI) is a dimensionless parameter introduced by He & Ku (Eq 13), with values near 0 indicating unidirectional flow, and values near 0.5 indicating highly oscillatory flow [55]. An *in vitro* study correlated increased particulate adhesion with elevated OSI [56].

$$\theta_i = \frac{1}{2}\left(1 - \frac{|\int_0^T \tau_w\, dt|}{\int_0^T |\tau_w|\, dt}\right) \tag{13}$$

where θ_i is the OSI. Another WSS based parameter commonly used to assess atherodegenerative conditions is the relative residence time (RRT), which provides a relative measure of the time blood spends in an arbitrary near-wall region [57], and is defined in Eq 14.

$$t_r = \frac{k}{(1-2\theta_i)\bar{\tau}_w} \tag{14}$$

where t_r is the RRT, and k is a proportionality constant arising from the near-wall assumption set as $k = 1$. Instead of simply reporting magnitudes of OSI and RRT, the percentage area of artery wall with values greater than the 66th percentile is instead quantified (OSI_{66} and RRT_{66} respectively) to allow for more meaningful comparisons of the disturbed hemodynamics between geometries, as described by De Nisco *et al.* [58].

In addition to these WSS based parameters, the time-averaged non-Newtonian importance factor (TANNIF) introduced by Ballyk *et al.* [59] is used to quantify the extent of non-Newtonian flow in the artery, with values outside of unity indicating highly non-Newtonian flow (Eq 15).

$$\bar{I}_L = \frac{1}{T}\int_0^T \frac{\mu}{\mu_N}\, dt \tag{15}$$

where $\bar{I}_L$ is the TANNIF and μ_N is the Newtonian viscosity listed in Table 1 (3.45 mPas). The final two parameters evaluated are based upon recent developments in correlating the vorticity induced flow disturbance to patient-specific artery models [60], comparing the increase in vorticity in healthy/diseased geometries to the type of plaques/lesions which develop. The time-average of the vorticity is taken over a cardiac cycle, and then averaged over the blood volume in the bifurcation ($\bar{\boldsymbol{\omega}}$), with the diseased vorticity index (DVI) being the difference in $\bar{\boldsymbol{\omega}}$ between the healthy/diseased cases (Eqs 16 and 17 respectively).

$$\bar{\omega} = \frac{1}{V}\int_0^V \frac{1}{T}\int_0^T |\omega| dt\, dV \tag{16}$$

$$V_D = \bar{\omega}_D - \bar{\omega}_H \tag{17}$$

where $\bar{\omega}$ is the volume average of the time-averaged vorticity and V_D is the DVI.

Solver settings

The solution to the above equations was obtained numerically via the discrete form of the SIMPLE algorithm for the pressure-velocity coupling, using a first order time discretisation scheme. All models were solved in parallel, utilising 120 cores on high performance computing nodes. To generate the hemodynamic parameters, each model was solved for a total of 3 cardiac cycles (2.4 s), with a time step of 1 ms, and all hemodynamic results being evaluated over the final cardiac cycle. The platelet model was then solved for an additional 4 s of flow time. Convergence criteria per iteration was set at a mass continuity residual $<10^{-4}$, and velocity residuals $<10^{-6}$ with the single and multiphase models taking an average wall clock time of 7 and 24 hours, respectively.

Mesh convergence

To ensure a mesh independent solution is obtained, simulations of the diseased bifurcation were performed at 7 incrementally increasing mesh refinements. These were performed as a steady-state simulation, using the maximum inlet velocity of 0.5 m/s. A final meshing criterion was selected once the percentage difference of peak blood velocity and average WSS on the bifurcation flow divider were both below 0.4% for each mesh refinement. The results of the convergence study are shown in Fig 5, with the final mesh consisting of 5.4 million mostly tetrahedral elements, with a 0.25 mm thick prismatic layer of 10 elements around the lumen walls for an accurate boundary layer formulation (Fig 6). The mesh has minimum, average and maximum edge length of 0.001, 0.1 and 0.175 mm respectively, with an average element skewness and orthogonal quality of 0.20 and 0.80, respectively [61].

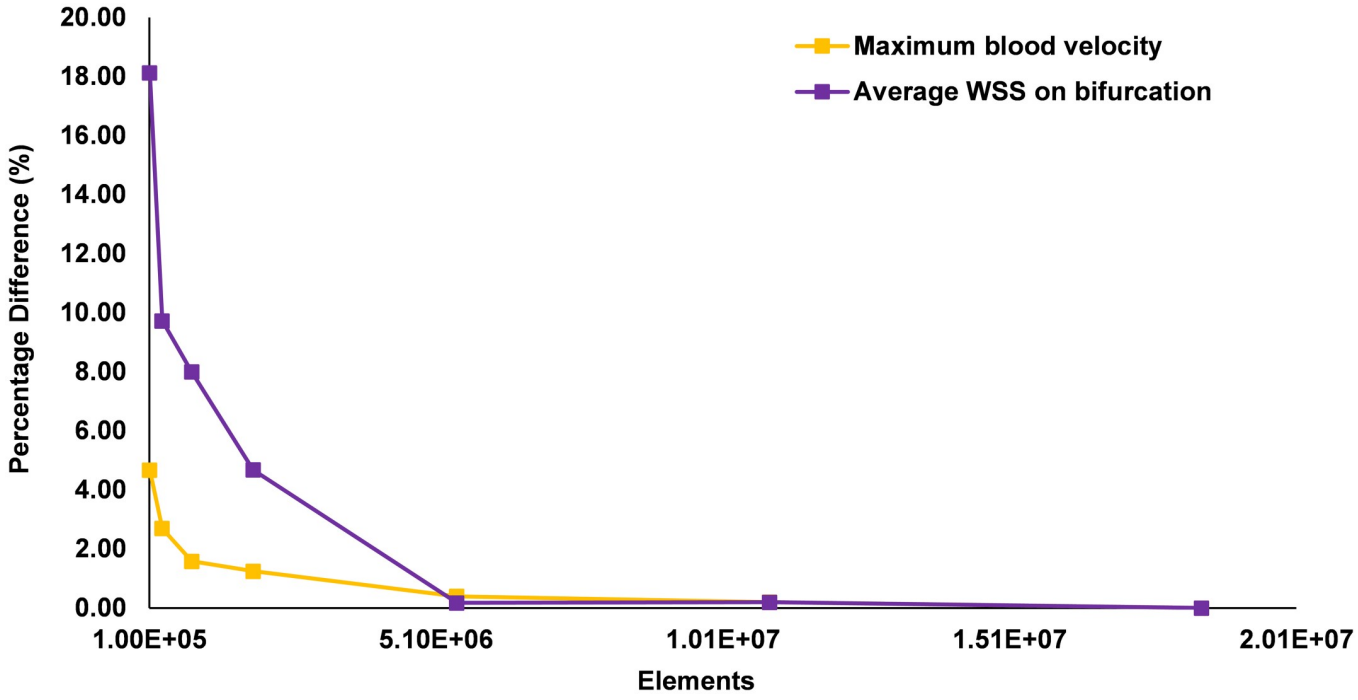

Fig 5. Percentage difference in peak velocity and bifurcation average wall shear stress for 7 mesh refinements.

https://doi.org/10.1371/journal.pone.0259196.g005

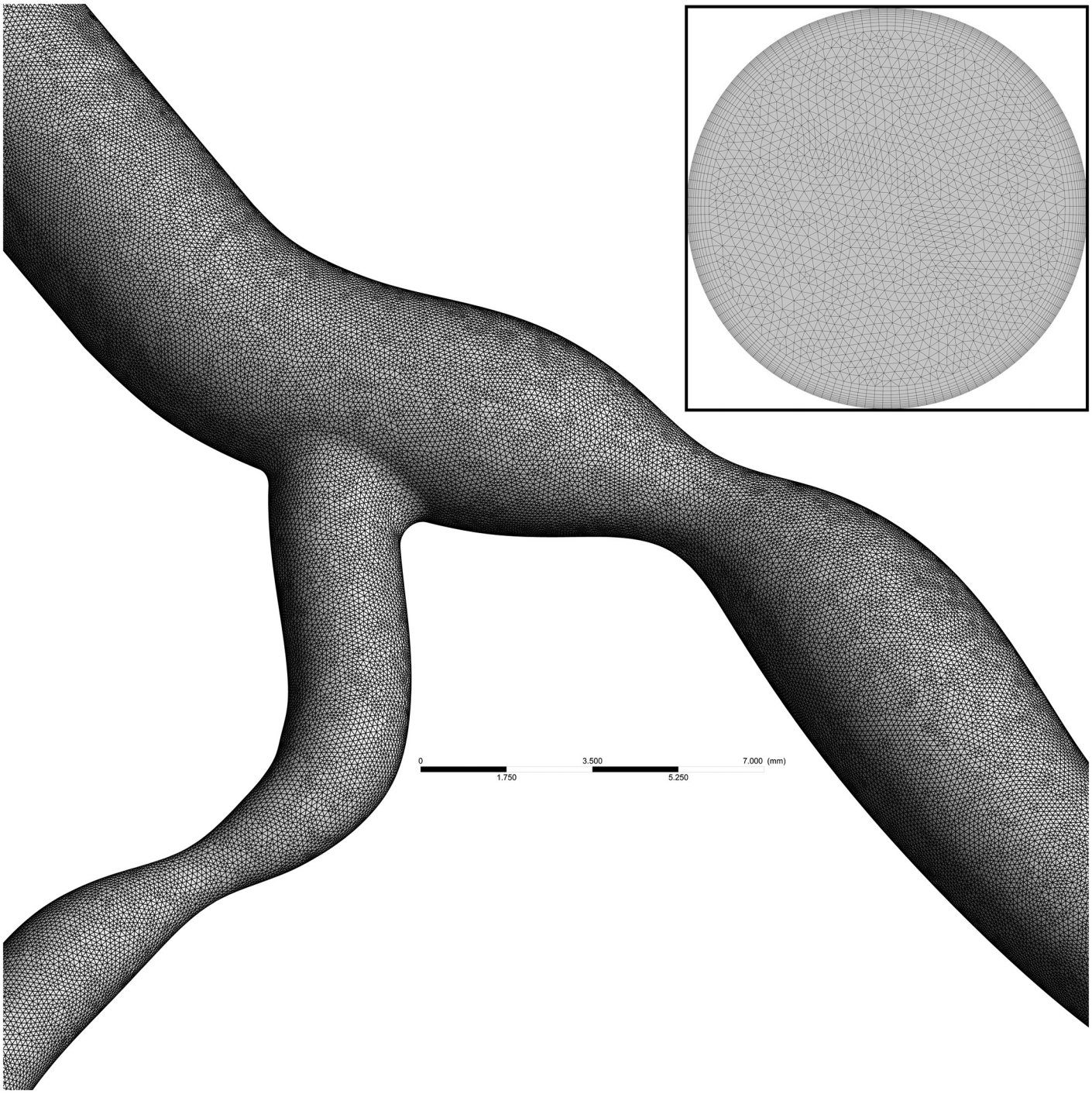

Fig 6. Mesh on surface of diseased coronary artery bifurcation and a cross section at inlet showing inflation layers near boundary.

https://doi.org/10.1371/journal.pone.0259196.g006

Results

The hemodynamics parameters defined previously were evaluated over the 3rd cardiac cycle for the healthy and diseased arteries and are reported in Table 3.

Table 3. Parameters averaged over the final cardiac cycle for the healthy and stenosed geometries (TA = time averaged).

Parameter	Healthy				Diseased			
	SN	SC	MN	MKM5	SN	SC	MN	MKM5
$\bar{\omega}$ (1/s)	234 ± 173	232 ± 173	227 ± 196	230 ± 179	275 ± 249	271 ± 248	259 ± 256	256 ± 227
DVI (mm^3/s)	-				4.15×10^5	3.90×10^5	3.22×10^5	2.58×10^5
TAWSS area < 1 Pa	9.48%	5.89%	5.56%	0.05%	15.09%	13.34%	10.54%	3.79%
OSI_{66}	0.92%	0.87%	0.78%	0.61%	3.81%	3.62%	3.20%	2.09%
RRT_{66}	5.14%	3.47%	3.31%	0.01%	11.32%	10.11%	8.23%	5.55%
Max TANNIF	1.00	3.96	1.08	2.68	1.00	13.10	1.09	6.27
Max TA Hematocrit	-		0.508	0.595	-		0.515	0.613
Min TA Hematocrit			0.321	0.204			0.282	0.167

https://doi.org/10.1371/journal.pone.0259196.t003

Shear stress parameters

All models show a consistent distribution of TAWSS around the bifurcation, with regions of low TAWSS localised on the outer walls, proximal to the bifurcation and distal to the stenosis (Fig 7). In the healthy artery, all models except the MKM5 show regions with pathologically low TAWSS <1 Pa. Single-phase models show consistently greater TAWSS, OSI_{66} and RRT_{66} values compared to the multiphase models, in particular the MKM5 model. Maximum values of TAWSS occur at the throat of the stenosis, with greatest values occurring in the LCx branch in all models. Despite allowing for RBC transport and phase interactions, the MN model performs most similarly to both single-phase approaches for TAWSS results.

The introduction of stenosis results in a moderate increase in areas with a pathologically low TAWSS for all models (+5.5% average), again with the MKM5's TAWSS results being smaller and localised closer to the stenosis (Fig 7). The SN model has the greatest results of all stress-based parameters throughout. Additionally, the TANNIF more than doubles for the SC and MKM5 models, indicating the presence of highly non-Newtonian flow in the diseased artery. Despite both the SC and MKM5 models both demonstrating non-Newtonian flow, the magnitude and distribution of TAWSS is still different, showing the importance of hematocrit on rheology and near-wall hemodynamics.

Vorticity

Results in terms of vorticity were consistent across all rheological models, with the largest difference from the Newtonian model being 2.2% (MN) and 5.2% (MKM5) in healthy and diseased arteries, respectively. The regions of disturbed flow result in a wide range of vorticity values, and hence the large standard deviation in values across the cycle. The disruption to the flow caused by the stenosis increased the vorticial nature of the flow for all models, with an average increase of 15%. The reduction in lumen diameter and increased shear at the throat of the stenosis is shown to increase the vorticity of the flow distal to the throat of the stenosis, separating from the wall and spreading across the artery (Fig 8). Multiphase models predict a more localised disruption to the vorticity, closer to the throat of the stenosis, with the flow normalising much sooner than in the two single-phase approaches. Multiphase models yielded a smaller DVI than the single-phase, with the MN and MKM5 having a difference of 22.4% and 37.8% from the single-phase Newtonian, respectively.

Hematocrit

To further analyse the differences between the two multiphase models, the distribution of hematocrit around the bifurcation in both the healthy and diseased cases is shown in Fig 9.

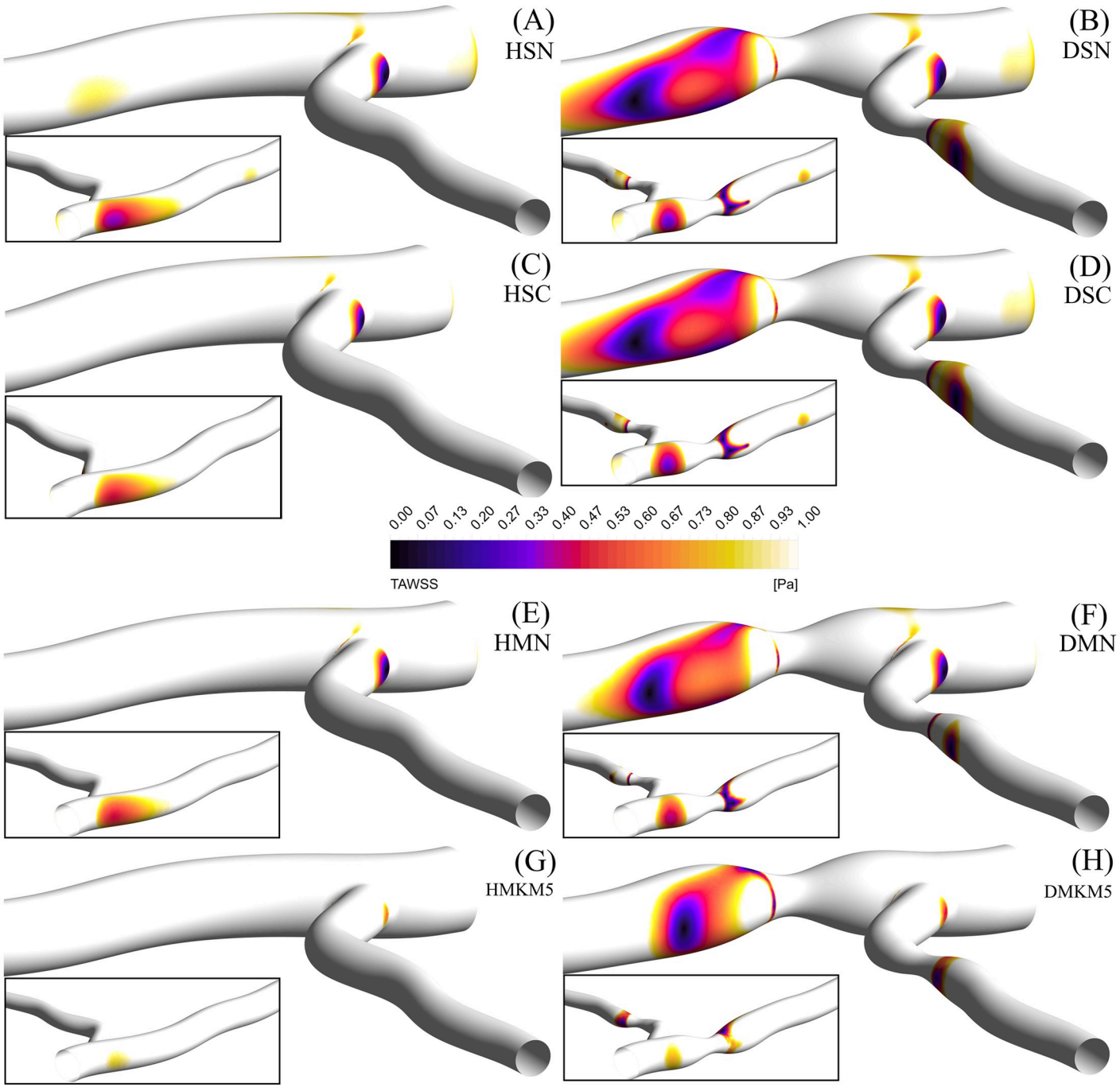

Fig 7. TAWSS contours of regions <1 Pa, for the left coronary bifurcation for the single Newtonian healthy (A) and diseased (B) cases, single Carreau healthy (C) and diseased (D) cases, multi Newtonian healthy (E) and diseased (F) cases, and the multi MKM5 healthy (G) and diseased (H) cases, with the reverse angle inlaid.

https://doi.org/10.1371/journal.pone.0259196.g007

Despite a uniform hematocrit inlet condition of 0.45 for both models, there is a significant difference in RBC concentration and hence phase transport between the two models. The MN model shows minimal deviation from the uniform distribution, even in the significantly disturbed flow occurring at the flow divider and the outer walls of the stenosis. The increased RBC transport arising in the MKM5 model predicts large regions of the artery with both

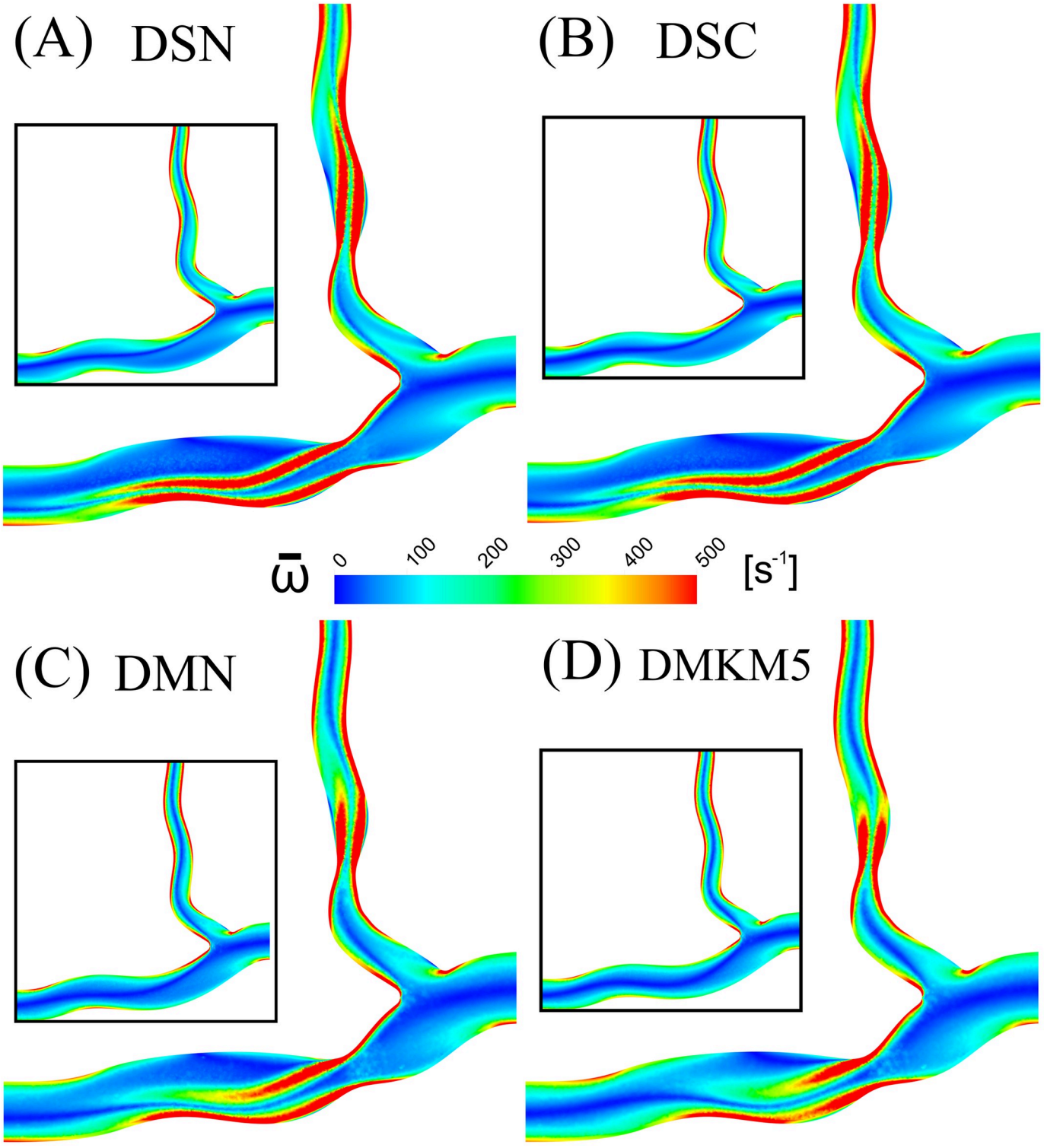

Fig 8. Mid-plane cross section of time averaged blood vorticity for the diseased artery: (A) Single-Newtonian, (B) Single-Carreau, (C) Multi-Newtonian and (D) Multi-MKM5 models.
Results for the healthy artery are inlaid as reference.

https://doi.org/10.1371/journal.pone.0259196.g008

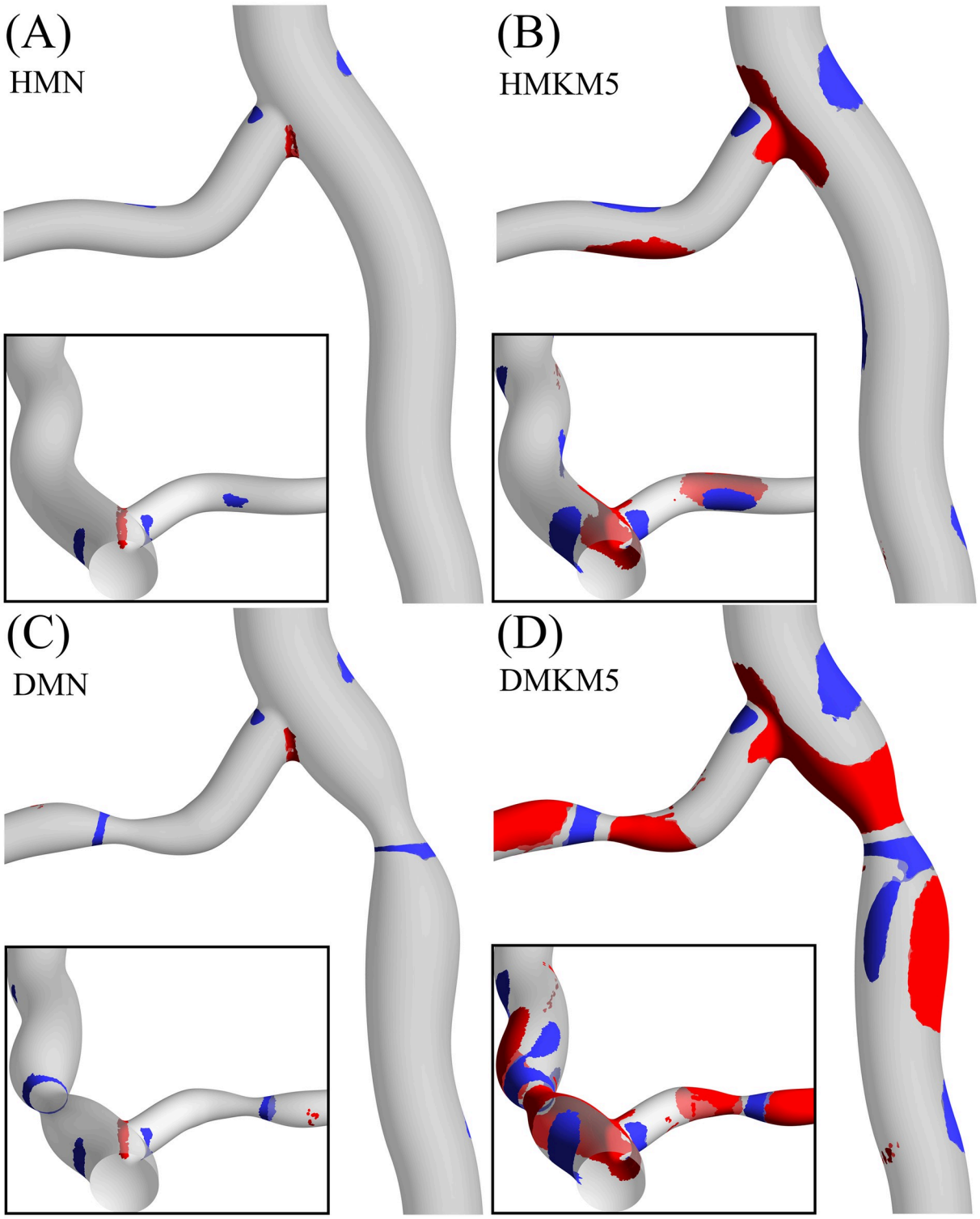

Fig 9. Red and blue iso-contours indicating regions of high (>0.5) and low (<0.4) TA hematocrit, respectively, for the healthy Multi-Newtonian (A) and Multi-MKM5 (B) models, and for the diseased Multi-Newtonian (C) and Multi-MKM5 (D) models, with reverse views inlaid.

https://doi.org/10.1371/journal.pone.0259196.g009

Table 4. Data from platelet tracking from the MKM5 model in the healthy/diseased artery.

Parameter	Healthy	Diseased
Platelets released across 1 cardiac cycle	106690	107512
Mean LOA (Pa.s)	2.91	3.13
Median LOA (Pa.s)	1.67	1.75
Mean residence time of all platelets (s)	1.08	1.20
Mean residence time for platelets with an elevated LOA (s)	1.47	1.53
Mean exposure time of platelets to low-shear ($<50\ s^{-1}$) aggregatory flow (s)	0.19	0.37

https://doi.org/10.1371/journal.pone.0259196.t004

increased and decreased hematocrit. As increased hematocrit will result in increased blood viscosity, these regions will experience elevated WSS and vice versa.

Platelet tracking

The platelet tracking model was implemented for the multiphase MKM5 model in the healthy and stenosed arteries, with results summarised in Table 4. The Lagrangian platelet residence time data has been used to extract regions in which the RBC shear rate is sufficiently low for aggregation ($<50\ s^{-1}$) and calculate the exposure time of platelets which are continuously exposed to this low-shear environment. This exposure time was reset to 0, if a platelet experienced a shear rate $>50\ s^{-1}$ for longer than 0.1 s to account for the effects of disaggregation. Videos of platelet flow, residence time, LOA and aggregatory exposure time are available in the (S1–S3 Figs).

The diseased artery has consistently greater levels of activation (~7%) than the healthy artery, with a large increase in the residence time of platelets which experience an elevated LOA in both the healthy (+36%) and diseased (+28%) arteries. The distribution of LOA and residence time across all platelets released can be seen in Fig 10.

In both arteries approximately 55% of platelets have residence times below 1 cardiac cycle, with platelets seeded in closest to the wall experiencing both the greatest residence times and LOA. Whilst platelets in the near-wall region have long RT in both arteries, the greater shear stress in the diseased artery results in consistently high LOA as seen in Fig 10a.

To evaluate the aggregatory potential of the low-shear environment around the bifurcation, the distributions of exposure time to sufficiently low RBC shear rates is shown in Fig 11. There is a distinct difference between the two arteries, with no platelets in the healthy artery exposed to aggregatory shear rates for greater than 0.7 s, compared to the maximum exposure of 2.9 s in the diseased artery occurring distal to the stenosis (Videos in S1–S3 Figs). The stenosis greatly increases the area of low-shear regions in the bifurcation which in turn increase the residence time of platelets and potentially RBC. The increased aggregatory potential in the diseased artery is highlighted in Fig 12B, showing localised recirculation of platelets in an ultra-low shear, high viscosity, high hematocrit, high residence time environment distal to the throat of the stenosis.

Discussion

This study presents for the first time, a Lagrangian platelet tracking model to assess the likely regions of platelet activation and hence indicate potential regions with an increased risk of clotting/thrombus formation alongside a comprehensive examination of the relation between blood rheology RBC aggregation/concentration and hemodynamics. Simulations of a porcine LAD/LCx stenotic bifurcation have shown the importance of non-Newtonian and multiphase

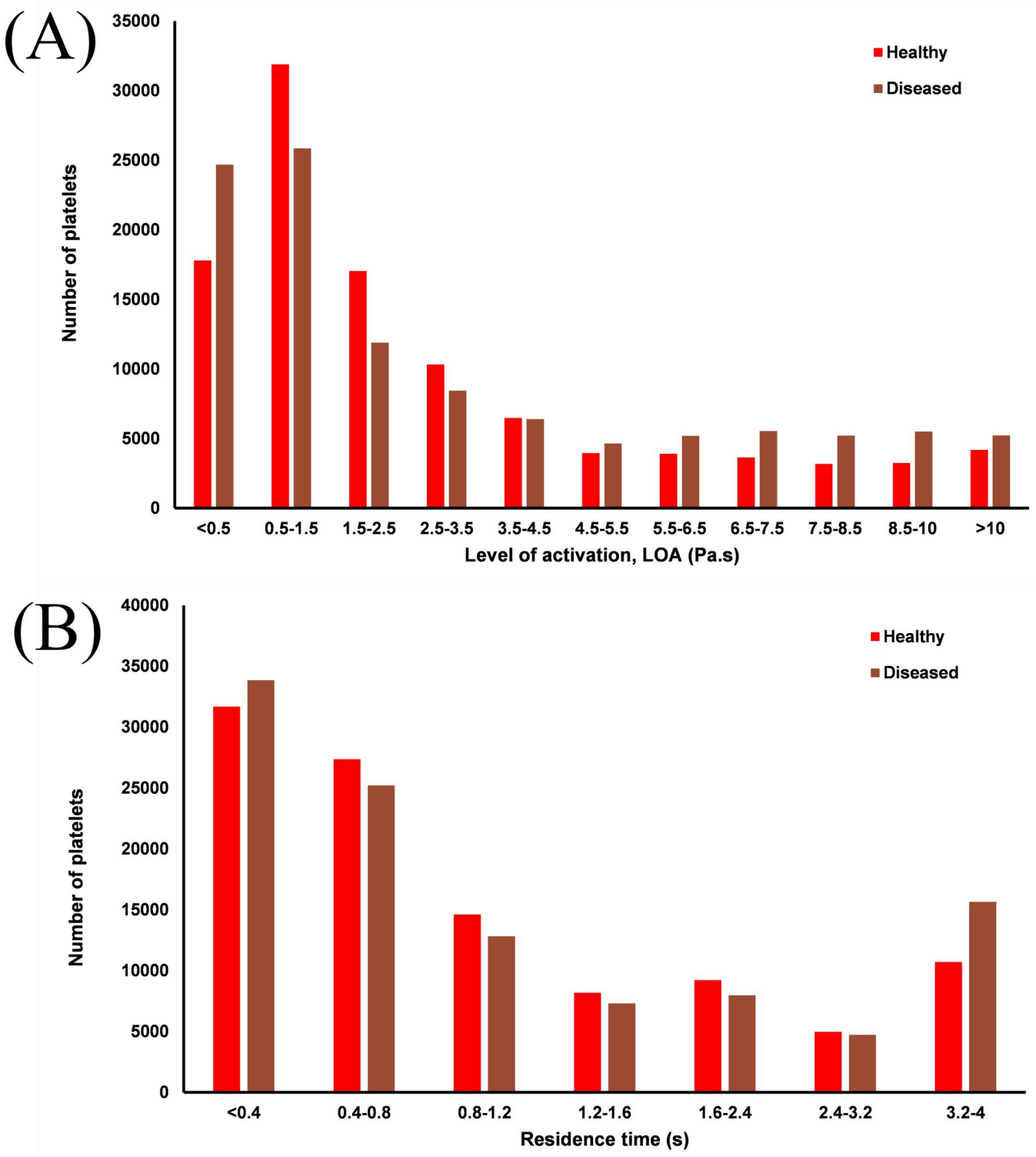

Fig 10. Bar charts showing distributions of LOA (A) and residence time (B) in both arteries.

https://doi.org/10.1371/journal.pone.0259196.g010

rheological properties on accurate predictions of parameters associated with atherosclerosis, with initial insights into how shear stress activation of platelets catalyses atherothrombosis.

Rheology and WSS

The links between WSS and atherosclerosis in coronary arteries have been well documented both *in vivo* and *in silico*, with regions of low TAWSS being associated with: plaque growth [62], reduced lumen diameter [53] and increased thrombus formation [63]. An *in vitro* study of coronary artery bifurcations of comparable branch angles also showed significant areas of low-shear and stagnation on the outer walls of the bifurcation [64] as seen in Fig 7. Additionally, an *in vivo* study of 506 patients with acute coronary syndrome confirmed the TAWSS patterns in Fig 7, with peak stresses occurring at the throat of stenosis, and increased regions of low TAWSS occurring 3–6 mm distal of the stenosis [53]. The increased RBC transport to these regions of stagnation distal to expansion [65] (Fig 9) is also associated with increased residence time of platelets (Fig 11) and atherogenic proteins which may further impair healthy endothelial function [66].

Of the four rheological approaches used in this study, three are based upon the viscometer data from Chien *et al.* [67], with the MKM5 model being fitted to the Brooks *et al.* [17] dataset. Discrepancies in the range of shear rates evaluated, hematocrit concentrations and temperature of blood combined with inherent limitations in measuring viscosity at the lowest shear rates [17] results in significant differences in predictions of blood viscosity across each model (Table 3). This significantly lower viscosity results in greater regions predicted to have a pathologically low TAWSS, with even the healthy bifurcation exhibiting large regions <1 Pa.

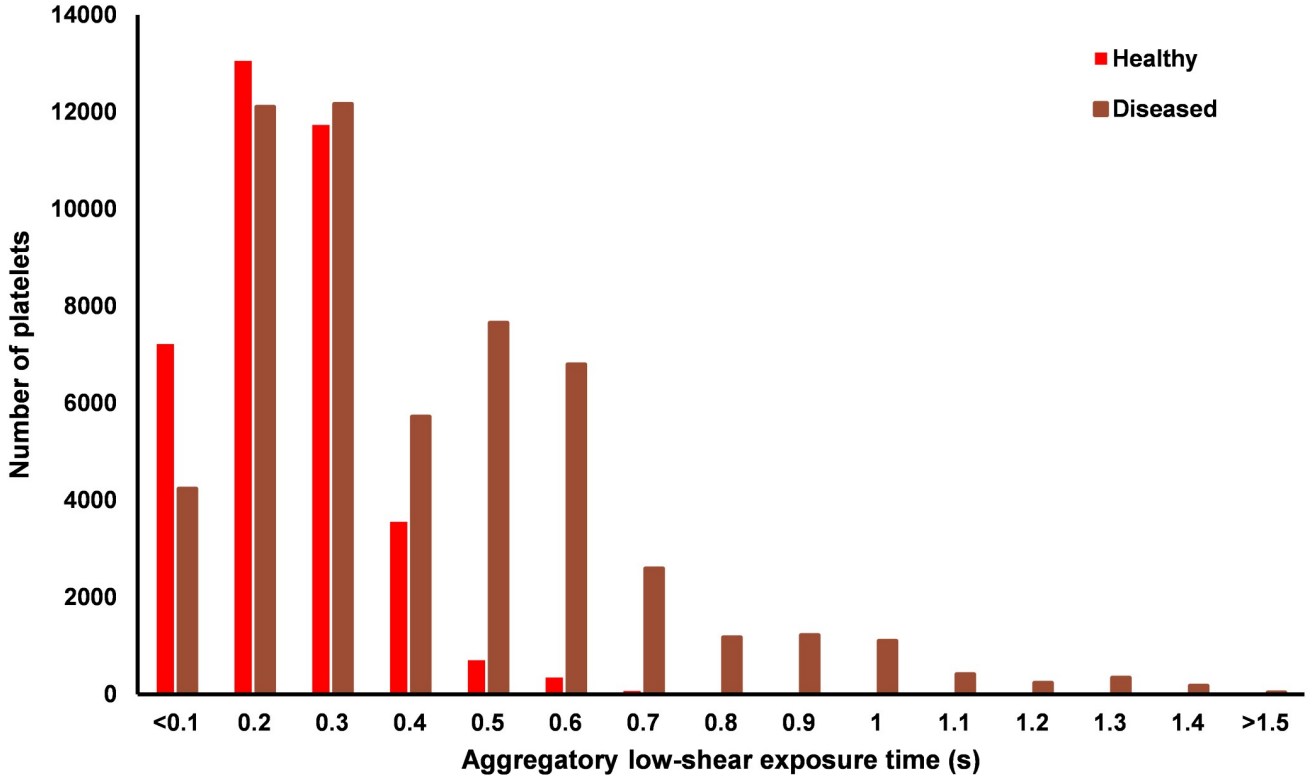

Fig 11. Bar chart showing the distribution of exposure time for the platelets which experienced a RBC shear rate <50 s^{-1}.

https://doi.org/10.1371/journal.pone.0259196.g011

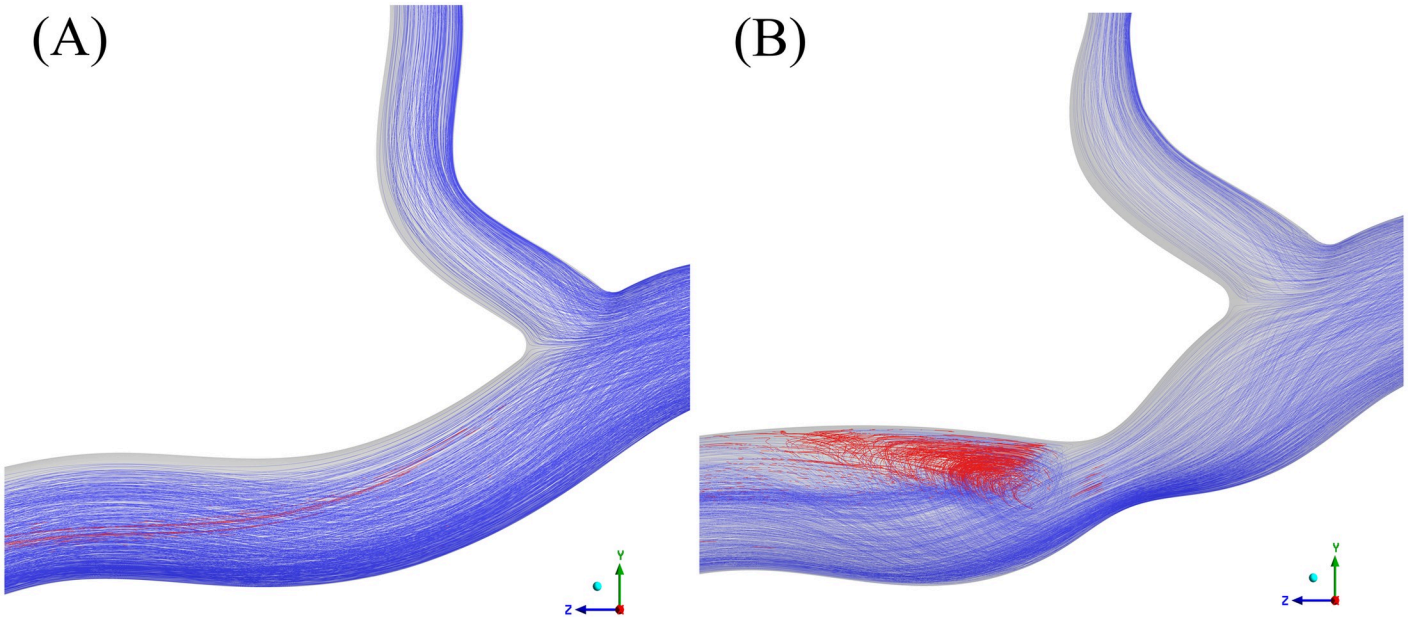

Fig 12. Platelet path lines for the healthy (A) and diseased (B) arteries, red indicates a low enough RBC shear rate for aggregation ($<50\ s^{-1}$).

https://doi.org/10.1371/journal.pone.0259196.g012

Furthermore, single-phase models will never be able to predict the non-Newtonian effects arising from RBC aggregation which is a key factor in non-Newtonian descriptors. Additionally in the diseased case, whilst distributions of TAWSS are similar across all models, the atherodegenerative regions are localised much closer to the stenosis (<6 mm) as demonstrated in Stone *et al.'s in vivo* study [53].

Vorticity

The vorticial nature of blood flow has been shown to impact cardiac function through multiple *in vivo* studies, with increased arterial vorticity arising in patients with right ventricular dysfunction [68]. Despite this link, coronary vorticity is thoroughly unexplored despite its potential as a non-invasive biomarker for assessing hemodynamic function [69]. The present study has demonstrated that the introduction of stenosis significantly increases the vorticity of coronary blood flow by 11–18% (across all models), with regions of high vorticity extending directly from the throat of the stenosis into the low-shear environments associated with atherosclerosis [70]. With DVI being correlated to the formation and geometry of atherosclerotic legions [60], the 38% lower value predicted by the MKM5 model compared to the SN model clearly shows the significance that RBC/plasma interactions have on flow disturbance. Based on Chu *et al.'s* patient-specific CFD study of coronary arteries [60], a lower DVI value may imply the growth of a more focal and severe lesion which correlates to the more localised TAWSS distribution of the MKM5 model immediately distal to the stenosis compared to the elongated SN distribution (Fig 7). Given these results and the variability in DVI with different rheology and phase models, it is therefore important to choose a sufficiently complex rheology/phase model which allows for a more accurate study of the severity of stenosis in coronary arteries.

Hematocrit and platelets

Despite both multiphase models utilising the same velocity and hematocrit boundary conditions, predictions in RBC transport and hematocrit vary extensively in both the healthy and stenosed arteries (Fig 9). The non-Newtonian behaviour of RBC in the MKM5 model is most significant in the near-wall region due to the wide range of shear rates and hematocrit occurring near the surface [30]. These fluctuations in hematocrit close to the surface will not only impact WSS magnitudes due to increased viscosity, but also affect platelet transport [71] which is strongly linked to interaction/collisions with RBC [72], hence the limited RBC transport of the multiphase Newtonian model is a significant limitation in accurately modelling blood rheology.

Evaluating the behaviour of platelets and their association with thrombus/clot formation is relevant for vascular pathologies [14, 73] (e.g. stenosis/aneurysms) but also the function of medical devices [36, 74] (e.g. catheters/stents). Platelet transport/activation is a complex process influenced by both mechanical factors such as shear stress [75], but also through biochemical reactions with proteins/agonists within the blood itself [76], with reviews of computational approaches by Anand & Rajagopal [77] and Yesudasan *et al.* [78]. The majority of platelet models focus on predicting thrombus formation and platelet behaviour through these biochemical interactions. However, the majority of these models focus on micro-scale flow [79, 80] which are poorly suited for the larger scale hemodynamics of this coronary bifurcation. Whilst the platelet model presented in this study lacks the biochemical activation potential of other models, its key benefit is linking the level of activation to prolonged residence times in specific 'at-risk' areas, to indicate likely regions for aggregation, sedimentation and clot formation in diseased arteries.

The seeding of platelets in the near-wall region shows platelets lingering around the bifurcation for multiple cardiac cycles in both arteries (S1–S3 Figs). Importantly the elevated blood shear stress at the throat of the stenosis and subsequent distal low-shear stagnation increases the LOA and creates the ideal environment for adhesion and clot growth. Platelets have long been associated with atherosclerosis [81], with *in vivo* studies showing their role in both the onset [10] and progression [6] of plaque growth. Additionally, the non-Newtonian effects of RBC aggregation are shown to be relevant in the diseased artery, with exposure time to sufficiently low-shear rates exceeding the approximate time ($>$1.5 s) for rouleuax formation to occur [21]. The resulting increase in the viscosity of blood will lead to further aggregation and sedimentation of erythrocytes distal to the stenosis, and is both symptomatic [82] and catalytic to the deterioration of the endothelium [83] and the development of atherothrombosis [84].

Limitations

The presented study was designed for the assessment of disease and rheology, however, there are several limitations/assumptions which impact the physiological accuracy. The principal limitations are from the geometry as it lacks some of the additional complexity and individuality arising from patient-specific scans [28, 85], including the vessel torsion which is one factor in the development of atheroprotective helical flow [86]. As applying boundary conditions of helical flow is not well documented, and whilst torsion is not directly associated with low WSS [58], the lack of helical flow development may impact hemodynamic predictions. Furthermore, only the main bifurcation branch was considered (LAD-LCx) as it is one of the most common locations for plaque growth [33], however, neglecting the additional downstream branches may alter pressure gradients and hence result in overestimation of WSS [87]. Despite this, the comparisons between rheological models are unbiased and unaffected.

Additional differences in flow boundary conditions arising from the implantation of stenosis could not be implemented in the model as adjusting the inlet condition without a suitable patient-specific profile would only further introduce errors/randomness and hence may limit differences between the two models.

The Lagrangian method of platelet simulation which determined activation only due to time-averaged shear stresses neglects the contribution of biochemical interactions in platelet activation. This discrete approach was chosen due to the macro-scale focus of this geometry and the inability of micro-scale (including majority of biochemical approaches) models to assess the trajectory, residence time and shear history of individual platelets.

Due to the sheer number of RBC in full sized arteries [22], individual RBC are not simulated in a Eulerian-Eulerian model, and so the effects of RBC deformation on their rheology/sedimentation cannot fully be included. Despite this, the momentum exchange coefficient (K_{ab}) between RBC/plasma is a function of Reynold's number/drag coefficient which will partially account for changes in shape due to flow conditions. With this study indicating aggregatory potential even in large arteries, we hope to expand current multiphase, macroscale rheology models to incorporate these aggregatory behaviours by linking factors such as: residence time, low-shear exposure and hematocrit to experimental rheometer measurements of RBC aggregates.

Conclusion

In this study, the choice of rheological model has been shown to strongly influence the assessment of coronary hemodynamic parameters. Single-phase models oversimplify crucial low-shear blood characteristics compared to the non-Newtonian multiphase model (MKM5) which provides a better representation of *in vivo* measurements. Whilst single-phase or Newtonian models may be acceptable for representing physiological undisturbed flow, the increased exposure time ($>$1.5 s) to aggregatory levels of low-shear in diseased arteries will impact crucial near-wall hemodynamics. Moreover, the wide ranges of hematocrit (0.163–0.617) and elevated vorticity (+15%) occurring distal to stenosis could impair the healthy function of the endothelium via pathological regions of TAWSS and the disruption of advection/diffusion of proteins/nutrients due to altered rheological properties. Additionally, the thrombogenic potential of stenotic arteries has been further classified, with platelets located in the near-wall region experiencing the highest LOA, and subsequently experiencing lengthier residence times (+32% increase) in the low-shear, stagnant region distal to the stenosis.

Supporting information

S1 Fig. Animation of platelet flow showing exposure to sufficiently low aggregatory shear levels ($<$50 s^{-1}) in the diseased MKM5 coronary artery bifurcation.
(MP4)

S2 Fig. Animation of platelet flow showing the residence time of platelets in the diseased MKM5 coronary artery bifurcation.
(MP4)

S3 Fig. Animation of platelet flow showing level of shear stress in the diseased MKM5 coronary artery bifurcation.
(MP4)

Acknowledgments

The authors would like to acknowledge the University of Birmingham BlueBEAR HPC service for computational resources.

Author Contributions

Conceptualization: David G. Owen, Diana C. de Oliveira, Emma K. Neale, Duncan E. T. Shepherd, Daniel M. Espino.

Data curation: David G. Owen.

Formal analysis: David G. Owen.

Methodology: David G. Owen, Diana C. de Oliveira, Emma K. Neale.

Project administration: Duncan E. T. Shepherd, Daniel M. Espino.

Software: David G. Owen.

Supervision: Duncan E. T. Shepherd, Daniel M. Espino.

Validation: David G. Owen.

Writing – original draft: David G. Owen.

Writing – review & editing: David G. Owen, Diana C. de Oliveira, Emma K. Neale, Duncan E. T. Shepherd, Daniel M. Espino.

References

1. Roth GA, Abate D, Abate KH, Abay SM, Abbafati C, Abbasi N, et al. Global, regional, and national age-sex-specific mortality for 282 causes of death in 195 countries and territories, 1980–2017: a systematic analysis for the Global Burden of Disease Study 2017. Lancet 2018. https://doi.org/10.1016/S0140-6736(18)32203-7.
2. Virani SS, Alonso A, Benjamin EJ, Bittencourt MS, Callaway CW, Carson AP, et al. Heart disease and stroke statistics—2020 update: A report from the American Heart Association. Circulation 2020. https://doi.org/10.1161/CIR.0000000000000757 PMID: 31992061
3. Dash D. Recent perspective on coronary artery bifurcation interventions. Heart Asia 2014; 6:18–25. https://doi.org/10.1136/heartasia-2013-010451 PMID: 27326157
4. Malek AM, Alper SL. Hemodynamic Shear Stress and Its Role in Atherosclerosis 2007; 282:2035–42.
5. Weber T, Auer J, O'Rourke MF, Kvas E, Lassnig E, Berent R, et al. Arterial Stiffness, Wave Reflections, and the Risk of Coronary Artery Disease. Circulation 2004; 109:184–9. https://doi.org/10.1161/01.CIR.0000105767.94169.E3 PMID: 14662706
6. Collet JP, Allali Y, Lesty C, Tanguy ML, Silvain J, Ankri A, et al. Altered fibrin architecture is associated with hypofibrinolysis and premature coronary atherothrombosis. Arterioscler Thromb Vasc Biol 2006; 26:2567–73. https://doi.org/10.1161/01.ATV.0000241589.52950.4c PMID: 16917107
7. Wentzel JJ, Chatzizisis YS, Gijsen FJH, Giannoglou GD, Feldman CL, Stone PH. Endothelial shear stress in the evolution of coronary atherosclerotic plaque and vascular remodelling: Current understanding and remaining questions. Cardiovasc Res 2012; 96:234–43. https://doi.org/10.1093/cvr/cvs217 PMID: 22752349
8. Louvard Y, Thomas M, Dzavik V, Hildick-Smith D, Galassi AR, Pan M, et al. Classification of coronary artery bifurcation lesions and treatments: Time for a consensus! Catheter Cardiovasc Interv 2008; 71:175–83. https://doi.org/10.1002/ccd.21314 PMID: 17985377
9. Chatzizisis YS, Coskun AU, Jonas M, Edelman ER, Feldman CL, Stone PH. Role of Endothelial Shear Stress in the Natural History of Coronary Atherosclerosis and Vascular Remodeling. Molecular, Cellular, and Vascular Behavior. J Am Coll Cardiol 2007; 49:2379–93. https://doi.org/10.1016/j.jacc.2007.02.059 PMID: 17599600
10. Badimon L, Padró T, Vilahur G. Atherosclerosis, platelets and thrombosis in acute ischaemic heart disease. Eur Hear J Acute Cardiovasc Care 2012; 1:60–74. https://doi.org/10.1177/2048872612441582 PMID: 24062891

11. Davi G, Patrono C. Platelet activation and atherothrombosis. N Engl J Med 2007; 357:2482–94. https://doi.org/10.1056/NEJMra071014 PMID: 18077812

12. Lee KE, Shin SW, Kim GT, Choi JH, Shim EB. Prediction of Plaque Progression in Coronary Arteries Based on a Novel Hemodynamic Index Calculated From Virtual Stenosis Method. Front Physiol 2019; 10:1–7.

13. Humphrey JD, Taylor CA. Intracranial and abdominal aortic aneurysms: Similarities, differences, and need for a new class of computational models. Annu Rev Biomed Eng 2008. https://doi.org/10.1146/annurev.bioeng.10.061807.160439.

14. Yazdani A, Li H, Humphrey JD, Karniadakis GE. A General Shear-Dependent Model for Thrombus Formation. PLoS Comput Biol 2017; 13:1–24. https://doi.org/10.1371/journal.pcbi.1005291 PMID: 28095402

15. Chaichana T, Sun Z, Jewkes J. Computation of hemodynamics in the left coronary artery with variable angulations. J Biomech 2011; 44:1869–78. https://doi.org/10.1016/j.jbiomech.2011.04.033 PMID: 21550611

16. Bessonov N, Sequeira A, Simakov S, Vassilevskii Y, Volpert V. Methods of Blood Flow Modelling. Math Model Nat Phenom 2016; 11:1–25. https://doi.org/10.1051/mmnp/201611101.

17. Brooks DE, Goodwin JW, Seaman GVF. Interactions among erythrocytes under shear. J Appl Physiol 1970; 28. https://doi.org/10.1152/jappl.1970.28.2.172 PMID: 5413303

18. Gidaspow D. Continuum and kinetic theory descriptions. Multiph. flow Fluid., 1994.

19. Eckmann DM, Bowers S, Stecker M, Cheung AT. Hematocrit, volume expander, temperature, and shear rate effects on blood viscosity. Anesth Analg 2000; 91:539–45. https://doi.org/10.1097/00000539-200009000-00007 PMID: 10960372

20. Galidi GP, Rannacher R, Robertson AM, Turek S. Hemodynamical Flows: Modeling, Analysis and Simulation. vol. 37. 2008.

21. Robertson AM, Sequeria A, Kameneva M V. Hemorheology. Hemodynamical Flows Model. Anal. Simul., 2008, p. 63–120.

22. Caro CG, Pedley TJ, Schroter RC, Seed WA, Parker KH. The mechanics of the circulation, second edition. 2011. https://doi.org/10.1017/CBO9781139013406.

23. Javadzadegan A, Yong ASC, Chang M, Ng MKC, Behnia M, Kritharides L. Haemodynamic assessment of human coronary arteries is affected by degree of freedom of artery movement. Comput Methods Biomech Biomed Engin 2017; 20:260–72. https://doi.org/10.1080/10255842.2016.1215439 PMID: 27467730

24. Chaichana T, Sun Z, Jewkes J. Computational fluid dynamics analysis of the effect of plaques in the left coronary artery. Comput Math Methods Med 2012; 2012. https://doi.org/10.1155/2012/504367.

25. Arzani A. Accounting for residence-time in blood rheology models: Do we really need non-Newtonian blood flow modelling in large arteries? J R Soc Interface 2018; 15. https://doi.org/10.1098/rsif.2018.0486 PMID: 30257924

26. Hund S, Kameneva M, Antaki J. A Quasi-Mechanistic Mathematical Representation for Blood Viscosity. Fluids 2017; 2:10. https://doi.org/10.3390/fluids2010010.

27. Soulis J V., Giannoglou GD, Chatzizisis YS, Seralidou K V., Parcharidis GE, Louridas GE. Non-Newtonian models for molecular viscosity and wall shear stress in a 3D reconstructed human left coronary artery. Med Eng Phys 2008; 30:9–19. https://doi.org/10.1016/j.medengphy.2007.02.001 PMID: 17412633

28. Lee SW, Steinman DA. On the relative importance of rheology for image-based CFD models of the carotid bifurcation. J Biomech Eng 2007; 129:273–8. https://doi.org/10.1115/1.2540836 PMID: 17408332

29. Johnston BM, Johnston PR, Corney S, Kilpatrick D. Non-Newtonian blood flow in human right coronary arteries: Transient simulations. J Biomech 2006; 39:1116–28. https://doi.org/10.1016/j.jbiomech.2005.01.034 PMID: 16549100

30. Owen DG, Schenkel T, Shepherd DE, Espino DM. Assessment of surface roughness and blood rheology on local coronary haemodynamics: a multi-scale computational fluid dynamics study. R Soc J Interface 2020; 17. https://doi.org/10.1098/rsif.2020.0327 PMID: 32781935

31. Jung J, Lyczkowski RW, Panchal CB, Hassanein A. Multiphase hemodynamic simulation of pulsatile flow in a coronary artery. J Biomech 2006; 39:2064–73. https://doi.org/10.1016/j.jbiomech.2005.06.023 PMID: 16111686

32. Dodge JT, Brown BG, Bolson EL, Dodge HT. Lumen diameter of normal human coronary arteries: Influence of age, sex, anatomic variation, and left ventricular hypertrophy or dilation. Circulation 1992; 86:232–46. https://doi.org/10.1161/01.cir.86.1.232 PMID: 1535570

33. Oviedo C, Maehara A, Mintz GS, Araki H, Choi SY, Tsujita K, et al. Intravascular ultrasound classification of plaque distribution in left main coronary artery bifurcations where is the plaque really located? Circ Cardiovasc Interv 2010; 3:105–12. https://doi.org/10.1161/CIRCINTERVENTIONS.109.906016 PMID: 20197513

34. Carty G, Chatpun S, Espino DM. Modeling Blood Flow Through Intracranial Aneurysms: A Comparison of Newtonian and Non-Newtonian Viscosity. J Med Biol Eng 2016; 36:396–409. https://doi.org/10.1007/s40846-016-0142-z.

35. Yilmaz F, Gundogdu MY. A critical review on blood flow in large arteries; relevance to blood rheology, viscosity models and physiologic conditions. Korea-Australia Rheol J 2008; 20:197–211. https://doi.org/10.1.1.462.7926.

36. Owen DG, De Oliveira DC, Qian S, Green NC, Shepherd DET, Espino DM. Impact of side-hole geometry on the performance of hemodialysis catheter tips: A computational fluid dynamics assessment. PLoS One 2020:1–16. https://doi.org/10.1371/journal.pone.0236946 PMID: 32764790

37. Ahmadi M, Ansari R. Computational simulation of an artery narrowed by plaque using 3D FSI method: influence of the plaque angle, non-Newtonian properties of the blood flow and the hyperelastic artery models. Biomed Phys Eng Express 2019; 5:045037. https://doi.org/10.1088/2057-1976/ab323f.

38. Yilmaz F, Kutlar AI, Gundogdu MY. Analysis of drag effects on pulsatile blood flow in a right coronary artery by using Eulerian multiphase model. Korea Aust Rheol J 2011; 23:89–103. https://doi.org/10.1007/s13367-011-0012-8.

39. ANSYS. Ansys Fluent 19.2 Theory Guide—Interfacial Area 2019. https://ansyshelp.ansys.com/account/secured?returnurl=/Views/Secured/corp/v192/flu_th/flu_th_sec_eulermp_theory_inter_area_conc.html (accessed April 1, 2020).

40. Schiller L, Naumann Z. A drag coefficient correlation. 1935.

41. Yilmaz F, Gundogdu MY. Analysis of conventional drag and lift models for multiphase CFD modeling of blood flow. Korea-Australia Rheol J 2009; 21:161–73.

42. ANSYS. Ansys Fluent 19.2 Theory Guide—Saffman Lift Force. 2019 2019. https://ansyshelp.ansys.com/account/secured?returnurl=/Views/Secured/corp/v192/flu_th/flu_th_sec_eulermp_lift.html (accessed April 1, 2020).

43. Ponder E. Hemolysis and related Phenomena. New York: Grune & Stratton; 1948.

44. Pal R. Rheology of concentrated suspensions of deformable elastic particles such as human erythrocytes. J Biomech 2003; 36:981–9. https://doi.org/10.1016/s0021-9290(03)00067-8 PMID: 12757807

45. Basciano C, Kleinstreuer C, Hyun S, Finol EA. A relation between near-wall particle-hemodynamics and onset of thrombus formation in abdominal aortic aneurysms. Ann Biomed Eng 2011; 39:2010–26. https://doi.org/10.1007/s10439-011-0285-6 PMID: 21373952

46. Morsi SA, Alexander AJ. An investigation of particle trajectories in two-phase flow systems. J Fluid Mech 1972; 55:193–208. https://doi.org/10.1017/S0022112072001806.

47. Kleinstreuer C, Feng Y. Computational analysis of non-spherical particle transport and deposition in shear flow with application to lung aerosol dynamics—A review. J Biomech Eng 2013;135. https://doi.org/10.1115/1.4023236 PMID: 23445053

48. Bluestein D, Niu L, Schoephoerster RT, Dewanjee MK. Fluid mechanics of arterial stenosis: Relationship to the development of mural thrombus. Ann Biomed Eng 1997; 25:344–56. https://doi.org/10.1007/BF02648048 PMID: 9084839

49. Dumont K, Vierendeels J, Kaminsky R, Van Nooten G, Verdonck P, Bluestein D. Comparison of the hemodynamic and thrombogenic performance of two bileaflet mechanical heart valves using a CFD/FSI model. J Biomech Eng 2007; 129:558–65. https://doi.org/10.1115/1.2746378 PMID: 17655477

50. Bénard N. Analyse de l'écoulement physiologique dans un stent coronarien: Application à la caractérisation des zones de resténose pariétale. Université de Poitiers, 2005.

51. Chabi F, Champmartin S, Sarraf C, Noguera R. Critical evaluation of three hemodynamic models for the numerical simulation of intra-stent flows. J Biomech 2015; 48:1769–76. https://doi.org/10.1016/j.jbiomech.2015.05.011 PMID: 26044195

52. Davies JE, Whinnett ZI, Francis DP, Manisty CH, Aguado-sierra J, Willson K, et al. Evidence of a Dominant Backward-Propagating "Suction" Wave Responsible for Diastolic Coronary Filling in Humans, Attenuated in Left Ventricular Hypertrophy 2006:59–61. https://doi.org/10.1161/CIRCULATIONAHA.105.603050.

53. Stone PH, Saito S, Takahashi S, Makita Y, Nakamura S, Kawasaki T, et al. Prediction of progression of coronary artery disease and clinical outcomes using vascular profiling of endothelial shear stress and arterial plaque characteristics: The PREDICTION study. Circulation 2012; 126:172–81. https://doi.org/10.1161/CIRCULATIONAHA.112.096438 PMID: 22723305

54. Samady H, Eshtehardi P, McDaniel MC, Suo J, Dhawan SS, Maynard C, et al. Coronary artery wall shear stress is associated with progression and transformation of atherosclerotic plaque and arterial remodeling in patients with coronary artery disease. Circulation 2011; 124:779–88. https://doi.org/10.1161/CIRCULATIONAHA.111.021824 PMID: 21788584

55. He X, Ku DN. Pulsatile flow in the human left coronary artery bifurcation: Average conditions. J Biomech Eng 1996; 118:74–82. https://doi.org/10.1115/1.2795948 PMID: 8833077

56. Chappell DC, Varner SE, Nerem RM, Medford RM, Alexander RW. Expression in Cultured Human Endothelium. Circ Res 1998; 82:532–9. https://doi.org/10.1161/01.res.82.5.532 PMID: 9529157

57. Himburg HA, Grzybowski DM, Hazel AL, LaMack JA, Li XM, Friedman MH. Spatial comparison between wall shear stress measures and porcine arterial endothelial permeability. Am J Physiol—Hear Circ Physiol 2004; 286:1916–22. https://doi.org/10.1152/ajpheart.00897.2003 PMID: 14715506

58. De Nisco G, Kok AM, Chiastra C, Gallo D, Hoogendoorn A, Migliavacca F, et al. The Atheroprotective Nature of Helical Flow in Coronary Arteries. Ann Biomed Eng 2019; 47:425–38. https://doi.org/10.1007/s10439-018-02169-x PMID: 30488307

59. Ballyk PD, Steinman DA, Ethier CR. Simulation of Non-Newitonian Blood Flow in an end to side anastomosis. Biorheology 1994; 31:565–86. https://doi.org/10.3233/bir-1994-31505 PMID: 7833458

60. Chu M, von Birgelen C, Li Y, Westra J, Yang J, Holm NR, et al. Quantification of disturbed coronary flow by disturbed vorticity index and relation with fractional flow reserve. Atherosclerosis 2018; 273:136–44. https://doi.org/10.1016/j.atherosclerosis.2018.02.023 PMID: 29501225

61. Shewchuk JR. What is a Good Linear Element? Interpolation, Conditioning, and Quality Measures. Elev Int Meshing Roundtable 2002:115–26. https://doi.org/10.1.1.68.8538.

62. Taylor CA, Steinman DA. Image-based modeling of blood flow and vessel wall dynamics: Applications, methods and future directions: Sixth international bio-fluid mechanics symposium and workshop, March 28–30, 2008 Pasadena, California. Ann Biomed Eng 2010; 38:1188–203. https://doi.org/10.1007/s10439-010-9901-0 PMID: 20087775

63. Stone PH, Coskun AU, Yeghiazarians Y, Kinlay S, Popma JJ, Kuntz RE, et al. Prediction of sites of coronary atherosclerosis progression: In vivo profiling of endothelial shear stress, lumen, and outer vessel wall characteristics to predict vascular behavior. Curr Opin Cardiol 2003; 18:458–70. https://doi.org/10.1097/00001573-200311000-00007 PMID: 14597887

64. Asakura T, Karino T. Flow patterns and spatial distributions of atherosclerotic lesions in human coronary arteries. Circ Res 1990; 66:1045–66. https://doi.org/10.1161/01.res.66.4.1045 PMID: 2317887

65. Karino T, Goldsmith HL. Adhesion of human platelets to collagen on the walls distal to a tubular expansion. Microvasc Res 1979; 17:238–62. https://doi.org/10.1016/s0026-2862(79)80002-3 PMID: 459938

66. Liepsch DW, Levesque M, Nerem RM, Moravec ST. Correlation of laser-Doppler-velocity measurements and endothelial cell shape in a stenosed dog aorta. Adv Exp Med Biol 1988; 242:43–50. https://doi.org/10.1007/978-1-4684-8935-4_6 PMID: 2977525

67. Chien S, Usami S, Taylor HM, Lundberg JL, Gregersen MI. Effects of hematocrit and plasma proteins on human blood rheology at low shear rates. J Appl Physiol 1966; 21:81–7. https://doi.org/10.1152/jappl.1966.21.1.81 PMID: 5903948

68. Hirtler D, Garcia J, Barker AJ, Geiger J. Assessment of intracardiac flow and vorticity in the right heart of patients after repair of tetralogy of Fallot by flow-sensitive 4D MRI. Eur Radiol 2016; 26:3598–607. https://doi.org/10.1007/s00330-015-4186-1 PMID: 26747260

69. Fenster BE, Browning J, Schroeder JD, Schafer M, Podgorski CA, Smyser J, et al. Vorticity is a marker of right ventricular diastolic dysfunction. Am J Physiol—Hear Circ Physiol 2015; 309:H1087–93. https://doi.org/10.1152/ajpheart.00278.2015 PMID: 26254331

70. Binu LS, Sukesh Kumar A. Simulation of left main coronary bifurcation lesions using 3D computational fluid dynamics model and its comparison with 2D. Lect. Notes Eng. Comput. Sci., vol. 2197, 2012, p. 631–6.

71. Wu WT, Aubry N, Massoudi M, Antaki JF. Transport of platelets induced by red blood cells based on mixture theory. Int J Eng Sci 2017; 118:16–27. https://doi.org/10.1016/j.ijengsci.2017.05.002.

72. AlMomani T, Udaykumar HS, Marshall JS, Chandran KB. Micro-scale dynamic simulation of erythrocyte-platelet interaction in blood flow. Ann Biomed Eng 2008; 36:905–20. https://doi.org/10.1007/s10439-008-9478-z PMID: 18330703

73. Rayz VL, Boussel L, Lawton MT, Acevedo-Bolton G, Ge L, Young WL, et al. Numerical modeling of the flow in intracranial aneurysms: Prediction of regions prone to thrombus formation. Ann Biomed Eng 2008; 36:1793–804. https://doi.org/10.1007/s10439-008-9561-5 PMID: 18787954

74. Gorbet MB, Sefton M V. Biomaterial-associated thrombosis: Roles of coagulation factors, complement, platelets and leukocytes. Biomaterials 2004; 25:5681–703. https://doi.org/10.1016/j.biomaterials.2004.01.023 PMID: 15147815

75. Anand M, Rajagopal K, Rajagopal KR. A model incorporating some of the mechanical and biochemical factors underlying clot formation and dissolution in flowing blood. J Theor Med 2003; 5:183–218. https://doi.org/10.1080/10273660412331317415.

76. Sorensen EN, Burgreen GW, Wagner WR, Antaki JF. Computational Simulation of Platelet Deposition and Activation: I. Model Development and Properties. Ann Biomed Eng 1999; 27:436–48. https://doi.org/10.1114/1.200 PMID: 10468228

77. Anand M, Rajagopal KR. A short review of advances in the modelling of blood rheology and clot formation. Fluids 2017; 2:1–9. https://doi.org/10.3390/fluids2030035.

78. Yesudasan S, Averett RD. Recent advances in computational modeling of fibrin clot formation: A review. Comput Biol Chem 2019; 83:107148. https://doi.org/10.1016/j.compbiolchem.2019.107148 PMID: 31751883

79. Wu WT, Jamiolkowski MA, Wagner WR, Aubry N, Massoudi M, Antaki JF. Multi-Constituent Simulation of Thrombus Deposition. Sci Rep 2017; 7:1–16.

80. Govindarajan V, Rakesh V, Reifman J, Mitrophanov AY. Computational Study of Thrombus Formation and Clotting Factor Effects under Venous Flow Conditions. Biophys J 2016; 110:1869–85. https://doi.org/10.1016/j.bpj.2016.03.010 PMID: 27119646

81. Farstad M. The role of blood platelets in coronary atherosclerosis and thrombosis. Scand J Clin Lab Invest 1998; 58:1–10. https://doi.org/10.1080/00365519850186779 PMID: 9516651

82. Goldstone J, Schmid-Schönbein H, Wells R. The rheology of red blood cell aggregates. Microvasc Res 1970; 2:273–86. https://doi.org/10.1016/0026-2862(70)90018-x PMID: 5523929

83. Massberg S, Brand K, Grüner S, Page S, Müller E, Müller I, et al. A critical role of platelet adhesion in the initiation of atherosclerotic lesion formation. J Exp Med 2002; 196:887–96. https://doi.org/10.1084/jem.20012044 PMID: 12370251

84. Viles-Gonzalez JF, Fuster V, Badimon JJ. Atherothrombosis: A widespread disease with unpredictable and life-threatening consequences. Eur Heart J 2004; 25:1197–207. https://doi.org/10.1016/j.ehj.2004.03.011 PMID: 15246637

85. Rabbi MF, Laboni FS, Arafat MT. Computational analysis of the coronary artery hemodynamics with different anatomical variations. Informatics Med Unlocked 2020; 19. https://doi.org/10.1016/j.imu.2020.100314.

86. Liu X, Pu F, Fan Y, Deng X, Li D, Li S. A numerical study on the flow of blood and the transport of LDL in the human aorta: The physiological significance of the helical flow in the aortic arch. Am J Physiol—Hear Circ Physiol 2009; 297:163–71. https://doi.org/10.1152/ajpheart.00266.2009.

87. Wiwatanapataphee B, Wu YH, Siriapisith T, Nuntadilok B. Effect of branchings on blood flow in the system of human coronary arteries. Math Biosci Eng 2012; 9:199–214. https://doi.org/10.3934/mbe.2012.9.199 PMID: 22229404